Research Article

Shaik Jakeer, Seethi Reddy Reddisekhar Reddy, Hayath Thameem Basha, Jaehyuk Cho*, and Veerappampalayam Easwaramoorthy Sathishkumar

Activation energy and Coriolis force impact on three-dimensional dusty nanofluid flow containing gyrotactic microorganisms: Machine learning and numerical approach

https://doi.org/10.1515/ntrev-2025-0179
received November 27, 2024; accepted May 12, 2025

Abstract: In recent times, machine learning methods have become powerful tools for solving complex problems, optimizing processes, and extracting insights from large datasets, especially in fluid dynamics. This study examines the effects of thermophoresis, Brownian motion, thermal radiation, and a non-uniform heat source on a dusty nanofluid containing gyrotactic microorganisms as it moves across a three-dimensional porous sheet. Additionally, the influence of activation energy and the Coriolis force on its biomechanics is investigated. MATLAB's bvp4c solver is used to solve the nonlinear equations governing velocity, temperature, concentration, and microbe density. The study also includes the computation of the skin friction coefficient and the heat transfer rate, with results presented in graphical form. Furthermore, key findings indicate that an augmentation in the fluid-particle interaction parameter results in a 12.5% increase in dust fluid velocity, whereas the fluid velocity diminishes by 9.8%. A 15% augmentation in the thermophoresis parameter improves temperature and concentration profiles by 10 and 8.7%, respectively. Furthermore, Brownian motion effects result in a 7.3% increase in temperature and a 5.2% reduction in concentration. The Nusselt number has a significant association with the thermophoresis parameter, especially at elevated levels, resulting in a 11.4% increase in heat transfer efficiency. Moreover, an increased concentration of dust particles leads to a 6.5% reduction in the temperature profile for both nanofluid and dusty fluid phases. The artificial neural network methodology effectively reduces computational time when solving complex fluid dynamics problems. This theoretical analysis has applications in various fields, including biodiesel and hydrogen synthesis, oil storage, geothermal energy extraction, base fluid mechanics, oil emulsification, food processing, renewable energy, and sewage treatment systems.

Keywords: machine learning approach, Coriolis force, motile microorganism's, dusty nanofluid, activation energy, radiation

*** Corresponding author: Jaehyuk Cho,** Department of Software Engineering & Division of Electronics and Information Engineering, Jeonbuk National University, Jeonju-Si, Republic of Korea, e-mail: chojh@jbnu.ac.kr
Shaik Jakeer: School of Technology, The Apollo University, Chittoor, A.P, 517127, India
Seethi Reddy Reddisekhar Reddy: Department of Mathematics, Koneru Lakshmaiah Education Foundation, Bowrampet, Hyderabad, 500043, Telangana, India
Hayath Thameem Basha: Department of Mathematical Sciences, Ulsan National Institute of Science and Technology (UNIST), Ulsan, Republic of Korea
Veerappampalayam Easwaramoorthy Sathishkumar: School of Engineering and Technology, Sunway University, No. 5, Jalan Universiti, Bandar Sunway, 47500, Selangor, Darul Ehsan, Malaysia

Abbreviations

C &C_p	concentration of the fluid and dust particles
$C_{Ax}\,Re_x^{1/2}/2$ & $C_{Ay}\,Re_x^{1/2}/2$	skin friction coefficients
c_m	specific heat dust particles (J/kg K)
c_{pf}	specific heat of fluid particles (J/kg K)
C_∞	ambient nanoparticles concentration
D_B	Brownian diffusion coefficient,
D_T	thermophoretic diffusion coefficient
E	non-dimensional activation energy
I	mass concentration of dusty particles
j	micro-inertia
$K = 6\pi\mu_f a$	Stokes drag constant
κ	vortex viscosity
k	thermal conductivity (W m^{-1} k^{-1})
k^*	mean absorption coefficient
Lb	bio convective Schmidt number

m	mass concentration of dust particles
N	dust particle's number density
N_B	Brownian motion parameter
N_T	thermophoresis parameter
$\mathrm{Nu}\,\mathrm{Re}_x^{-1/2}$	Nusselt number
Pe	Peclet number
Pr	Prandtl number
Re_x	local Reynolds number
Rd	thermal radiation
Sc	Schmidt number
T &T_p	temperature of the fluid and dust particles
T_w	wall temperature (K)
T_∞	temperature of the ambient fluid
v_1, v_2 & v_3	velocity component along x, y, & z-direction
x, y & z	Cartesian coordinates (m s^{-1})
τ_T	thermal equilibrium time

Greek symbols

α	rotational parameter
β_v	fluid–particle interaction parameter
τ_2	temperature jump parameter
ρ	density (kg m^{-3})
γ	ratio of specific heat
η	similarity variable
μ	dynamic viscosity (kg m^{-1} s^{-1})
υ	kinematic viscosity (m^2 s^{-1})
θ	dimensionless temperature
β_t	fluid–particle interaction parameter for temperature
β_c	fluid–particle interaction parameter for concentration

Subscripts

f	fluid

1 Introduction

Bioconvection is a naturally occurring phenomena that mostly includes the dispersion of self-propelled microorganisms in the field of fluid dynamics. Bioconvection is distinct from conventional multi-phase flows because it is characterized by molecules that are not self-propelled, but rather propelled by the fluid flow, in contrast to typical multi-phase flows. These microorganisms have a tendency to move upwards in the top section of the fluid, where there is a concentration that leads to instability because of the large difference in density. These self-propelled motile organisms have a tendency to convene at the apex of the liquid stratum, causing the top layer to become more denser than the bottom region. This imbalance in density ultimately results in system instability [1–4]. The nanoparticles in the nanofluid are moved by the Brownian motion and thermophoresis, unlike motile microorganisms, which are capable of self-propulsion. Consequently, the movement of the nanoparticles is not connected to the motion of the bacteria. The motile microorganisms can be classified into various types based on their impellent, such as oxytocic, gyrotactic, and negative gravities microorganisms. Microorganisms are of great importance in the fields of engineering, biology, medicine, and the environment, both in theoretical and applied study. Examples of applications in environmental and biological sciences include the ability to absorb CO_2 more efficiently than agricultural crops, waste treatment plants, heterogeneous catalysis, the production of biodiesel, ethanol, and fertilizers, bacterially optimized petroleum and natural gas retrieval systems, production of food, chemotherapy for cancer, and the utilization of enzyme biomaterials in bio-microsystems [5–11]. Ahmad *et al.* [12] examined the unique characteristics of hybrid nanoparticles, such as manganese zinc ferrite and nickel zinc ferrite, in the movement of motile gyrotactic bacteria in a bio-convective flow. This flow occurs in a media known as Darcy Forchheimer. Dey and Chutia [13] examined the flow of a nanofluid including dust particles across a vertically stretched flat surface, considering the presence of a two-phase bio-convective system. Agarwal *et al.* [4] investigated mass and heat transfer in nanofluid flow inside the Powell-Eyring model across an exponentially stretched sheet containing motile microorganisms. Rajeswari and De [14] investigated the point at which tetra-hybrid nanofluid blood flow reaches a state of standstill on a vertical stretched cylinder using bioconvection. Loganathan *et al.* [15] investigated the bioconvective gyrotactic microorganisms in third-grade nanofluid flow over a Riga surface, focusing on stratification and entropy formation. Loganathan *et al.* [16] investigated the dynamics of Ree-Eyring nanofluid under the influences of free convection, bioconvection, heat source, and thermal radiation on a convection-heated Riga plate. Rashed *et al.* [17] used thermophoresis and Brownian motion to investigate the bioconvective flow around a tiny surgical needle in blood containing ternary hybrid nanoparticles.

The formation of the dusty fluid (DF) occurs as a result of the interaction between the base liquid and the minute

particles, which are commonly measured in microns or millimeters. Airborne dust consists of little desiccated particles. When a fluid with lower viscosity has solid particles dispersed in it, the movement of this fluid through the system will lead to the creation of a DF. A prominent illustration of the issue of dusty air is the phenomenon of fluidization, which transpires when minuscule dust particles aggregate, resulting in the formation of precipitation. When referring to the pace at which dust velocity shifts, the word "relaxation time" is the term that is employed. To determine the relaxation time, it is essential to first get the particle scale. Furthermore, Fortov *et al.* [18] produced evidence that demonstrated that the forces exerted by dust on gas particles and on other dust particles are comparable. To stress the fact that dusty plasma is a sort of ionized gas that contains tiny charged condensed particles, it is essential to accentuate this property. Because of the significance of dust particles that are carried in the air, a significant number of experts have made contributions to the database of information that is now available. In in the context of the present situation and the increasing concerns about needs in the mechanical, industrial, technical, and medical domains, experts in these fields have called for the use of DF. This fluid has many real-world uses, such as in cancer detection and treatment, in assessing its interactions with living things, in studying lunar thermal plant ash, in analyzing metal objects coated with polymers, and in helping to dry solids, especially for the cultivation of beneficial microbes. To mention a few of its various applications, it is used in fuel transportation, air conditioner cooling, crude oil purification, and for the manufacturing of granulated polyethylene power station pipes [19–27]. Imitaz *et al.* [28] evaluated the moving mechanics of blood flow in a cylinder with magnetic dust particles. The effect of a fluctuating pressure gradient allowed this to be achieved. Nawaz and colleagues [29] investigated the transmission of thermal energy that results from the dispersion of both single and blended nanoparticles in a hyperbolic fluid with a tangent that contains dust particles. When it comes to dust particles, the hybrid nanofluid is cooler than that nanofluid. All of this was based on their findings.

The fundamental criterion for mass transmission is characteristically not satisfied in chemical reactions that occur at the species level and have constrained Arrhenius activation energies (AAE). Within the context of this discussion, the term "Activation Energy" (AAE) refers to the minimal quantity that must be present in order to initiate a chemical reaction between atoms or molecules that are present in a chemical system. A Swedish scientist named Svante Arrhenius is credited with coining the term "activation energy" in the year 1889. When the fundamental equation for mass conservation is solved, it is possible to easily determine the impact that mass transfer has on the reaction. The use of chemical processes, including AAE, is commonplace in a variety of domains, including oil reservoir engineering, food production, and geothermal theory [30–32]. Ansys CFX software is a commercially available computational fluid dynamics (CFD) tool that is highly successful in tackling difficult chemical kinetics problems. The development of this system was specifically intended to address complex computational issues related to chemical processes [33]. Khan *et al.* [34] employed electromagnetic hydrodynamics to study the effect of an AAE chemical reaction on the Casson fluid flow at a point of stagnation on an extended surface. Khan *et al.* [35] did a study to examine how in the case of the Casson nanofluid, the nonlinear radiative mixed convective flow over a stretched surface was influenced by both the chemical process and the AAE. Shafique *et al.* [36] conducted a research examining transport of Maxwell nanofluid in three dimensions throughout a stretched medium. The researchers considered the presence of Arrhenius activation energy and chemical reaction. The observed activation energy (AAE) rose, resulting in a decline in solute concentration and therefore reducing the mass flow across the wall. The magnitude of these drops becomes more severe as the distance between the wall and the temperature of the surrounding environment decreases. The investigation conducted by Reddy *et al.* [37] showed that the activation energy has an impact on exothermic chemical processes involving the 3D-MHD slip flow of a Powell-Eyring fluid across a thin surface. Gomathi and Poulomi [38] investigated the dual Casson Williamson nanofluid including radiation and chemical processes on a stretching/shrinking sheet. Mabrouk *et al.* [39] investigated how motile microorganisms affect the bioconvection of unstable nonhomogeneous hybrid nanofluids.

The primary purpose of this model is to explore the heat transmission properties of a nanofluid that is classified as dusty and contains gyrotactic microorganisms on a surface that is three-dimensional. This inquiry will occur in the context of linear thermal radiation and non-uniform heat sources and sinks. No previous studies have investigated the impact of Coriolis force and activation energy on a three-dimensional porous surface when exposed to a dusty nanofluid (DNF) containing gyrotactic microorganisms. This has been substantiated by previous study. In order to solve this model, the equations governing the transfer of flow temperature and concentration are transformed into an ordinary differential system by implementing the necessary self-similarity transformations. This method goes beyond the conventional numerical and empirical methodologies by using a multi-layer artificial neural network (ANN) with MLP

feed-forward backpropagation and the Levenberg-Marquardt algorithm. Using the state-of-the-art bvp4c solution in MATLAB, the complicated system of nonlinear equations controlling skin friction, heat transfer rate, velocity, and temperature is solved.

- What effects do the Coriolis force and activation energy have on a DF temperature, concentration, and velocity profiles?
- How do the characteristics of the fluid-particle interaction affect the rates of mass and heat transfer?
- What is the impact of thermophoresis, Brownian motion, and permeability parameters on the thermal and microbiological properties of nanofluids?
- Can ANNs enhance the efficiency and precision of solving nonlinear differential equations in fluid dynamics relative to traditional numerical methods?
- What is the impact of gyrotactic microorganisms on the stability and heat transfer properties of the DNF system?

2 Formulation of the problem

The study focuses on a stable, three-dimensional, incompressible nanofluid containing dust particles. The nanofluid is subjected to a non-uniform heat source/sink and thermal radiation while being stretched on a surface. A constant velocity speed, denoted by the letter Ω, is maintained during the rotational motion of the fluid all over z-axis (Figure 1). The various characteristics of the Coriolis force are represented by the first and second momentum equations, which are denoted by the letters $-2\Omega v_2$ and $2\Omega v_1$, respectively. The Buongiorno nanofluid model incorporates the influences of thermophoresis and Brownian motion. The considerations of activation energy, heat radiation, and chemical reactions are also included. It is believed that the stream of dust consists of spheres that are of the same size and density. T_∞ for the fluid around the extended sheet and T_w for the sheet itself are the temperatures, respectively, of this system. In this case, the nonlinear differential equations may be derived by taking into account the problem constraints and the accurate factors for the surface flow [40].

2.1 Fluid phase

$$\frac{\partial v_1}{\partial x} + \frac{\partial v_2}{\partial y} + \frac{\partial v_3}{\partial z} = 0, \tag{1}$$

$$v_1\frac{\partial v_1}{\partial x} + v_2\frac{\partial v_1}{\partial y} + v_3\frac{\partial v_1}{\partial z} - 2\Omega v_2 = \upsilon_f\frac{\partial^2 v_1}{\partial z^2} + \frac{KN}{\rho_f}(v_{1p} - v_1) - \frac{\upsilon_f}{k_1}v_1, \tag{2}$$

$$v_1\frac{\partial v_2}{\partial x} + v_2\frac{\partial v_2}{\partial y} + v_3\frac{\partial v_2}{\partial z} + 2\Omega v_1 = \upsilon_f\frac{\partial^2 v_2}{\partial z^2} + \frac{KN}{\rho_f}(v_{2p} - v_2) - \frac{\upsilon_f}{k_1}v_2, \tag{3}$$

$$v_1\frac{\partial T}{\partial x} + v_2\frac{\partial T}{\partial y} + v_3\frac{\partial T}{\partial z} = \alpha_f\left(\frac{\partial^2 T}{\partial z^2}\right) + \tau\left[D_B\frac{\partial C}{\partial z}\frac{\partial T}{\partial z} + \frac{D_T}{T_\infty}\left(\frac{\partial T}{\partial z}\right)^2\right] + \frac{mNc_{pf}}{\tau_T(\rho c_p)_f}(T_p - T) - \frac{1}{(\rho c_p)_f}\frac{\partial q_r}{\partial z} + \frac{q'''}{(\rho c_p)_f}, \tag{4}$$

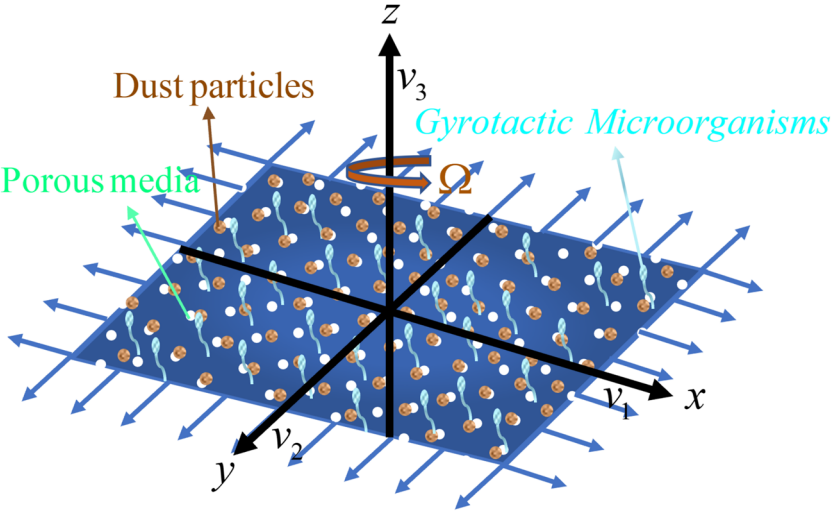

Figure 1: Schematic diagram and coordinate system.

$$v_1\frac{\partial C}{\partial x} + v_2\frac{\partial C}{\partial y} + v_3\frac{\partial C}{\partial z} = D_B\frac{\partial^2 C}{\partial z^2} + \frac{D_T}{T_\infty}\frac{\partial^2 T}{\partial z^2} + \frac{mN}{\rho_f \tau_C}(C_p - C) - \gamma_0^2(C - C_\infty)\left(\frac{T}{T_\infty}\right)^{n_1}\exp\left(-\frac{E_0}{k^*T}\right), \tag{5}$$

$$v_1\frac{\partial N}{\partial x} + v_2\frac{\partial N}{\partial y} + v_3\frac{\partial N}{\partial z} + \frac{bW}{(C_w - C_\infty)}\frac{\partial}{\partial y}\left(N\frac{\partial C}{\partial y}\right) = D_m\frac{\partial^2 N}{\partial y^2}. \tag{6}$$

2.2 Dusty phase

$$\frac{\partial v_{1p}}{\partial x} + \frac{\partial v_{2p}}{\partial y} + \frac{\partial v_{3p}}{\partial z} = 0, \tag{7}$$

$$v_{1p}\frac{\partial v_{1p}}{\partial x} + v_{2p}\frac{\partial v_{1p}}{\partial y} + v_{3p}\frac{\partial v_{1p}}{\partial z} = \frac{K}{m}(v_1 - v_{1p}), \tag{8}$$

$$v_{1p}\frac{\partial v_{2p}}{\partial x} + v_{2p}\frac{\partial v_{2p}}{\partial y} + v_{3p}\frac{\partial v_{2p}}{\partial z} = \frac{K}{m}(v_2 - v_{2p}), \tag{9}$$

$$v_{1p}\frac{\partial T_p}{\partial x} + v_{2p}\frac{\partial T_p}{\partial y} + v_{3p}\frac{\partial T_p}{\partial z} = \frac{c_p}{c_m\tau_T}(T - T_p), \tag{10}$$

$$v_{1p}\frac{\partial C_p}{\partial x} + v_{2p}\frac{\partial C_p}{\partial y} + v_{3p}\frac{\partial C_p}{\partial z} = \frac{c_p}{c_m\tau_C}(C - C_p). \tag{11}$$

The boundary conditions:

$$\left.\begin{aligned} &v_1 = ax,\ v_2 = 0,\ v_3 = 0,\ T = T_w,\ C = C_w,\ N = N_w,\\ &\text{at } z = 0,\\ &v_1 \to 0,\ v_2 \to 0,\ T \to T_\infty,\ C \to C_\infty,\ N \to N_\infty,\\ &v_{1p} \to 0,\ v_{2p} \to 0,\ v_{3p} \to v_3,\ T_p \to T_\infty,\ C_p \to C_\infty,\\ &\text{as } z \to \infty. \end{aligned}\right\} \tag{12}$$

where x, y, and z are the Cartesian coordinates, v_1, v_2, and v_3 are the fluid velocity components and v_{1p}, v_{2p}, and v_{3p} are the dust particle velocities along x, y, and z-directions, υ_f is the kinematic viscosity, μ_f is the dynamic viscosity of the fluid, k_1 is the permeability parameter, γ_0 is the reaction rate, D_T is the thermophoretic diffusion coefficient, D_B is the Brownian diffusion coefficient, n_1 is the exponent fitted rate constant, E_0 is the dimensional form of activation energy, k^* is the Boltzmann constant, τ_C is the concentration equilibrium time, $\tau = \frac{(\rho c_p)_p}{(\rho c_p)_f}$ is the capacity ratio, c_{pf} is the specific heat of fluid, c_{p_p} is the specific heat of particle, ρ_f is the density of the fluid, ρ_p is the density of the particle, and c_m is the specific heat dust particles.

Equation (6) provides the radiative heat flow as

$$q_r = -\frac{4\sigma^*}{3k^*}\frac{\partial T^4}{\partial z}. \tag{13}$$

The model for the non-uniform heat source and sink, q''', is

$$q''' = \frac{k_f u_w}{x\upsilon_f}\left(A(T_w - T_\infty)\frac{d}{d\eta}G_1'(\eta) + B(T - T_\infty)\right). \tag{14}$$

The similarity transformations are as follows:

$$\left.\begin{aligned} &v_1 = axG'_1(\eta),\ v_2 = axG_2(\eta),\ v_3 = -\sqrt{a\upsilon}\,G_1(\eta),\\ &\eta = \left(\frac{a}{\upsilon}\right)^{1/2} z,\\ &v_{1p} = axg_1'(\eta),\ v_{2p} = axg_2(\eta),\ v_{3p} = -\sqrt{a\upsilon}\,g_1(\eta),\\ &\chi(\eta) = \frac{N - N_\infty}{N_w - T_\infty},\\ &\theta = \frac{T - T_\infty}{T_w - T_\infty},\ \phi = \frac{C - C_\infty}{C_w - C_\infty},\ \theta_p = \frac{T_p - T_\infty}{T_w - T_\infty},\\ &\phi_p = \frac{C_p - C_\infty}{C_w - C_\infty}. \end{aligned}\right\} \tag{15}$$

Using equation (15), equations (2)–(11) are transformed into the following form:

2.3 Fluid phase

$$\left(\frac{d}{d\eta}G_1(\eta)\right)^2 - G_1(\eta)\frac{d^2}{d\eta^2}G_1(\eta) - 2\alpha G_2(\eta) = \frac{d^3}{d\eta^3}G_1(\eta) + I\beta_v\left(\frac{d}{d\eta}g_1(\eta) - \frac{d}{d\eta}G_1(\eta)\right) - \Upsilon\frac{d}{d\eta}G_1(\eta), \tag{16}$$

$$G_2(\eta)\frac{d}{d\eta}G_1(\eta) - \left(\frac{d}{d\eta}G_2(\eta)\right)G_1(\eta) + 2\alpha\frac{d}{d\eta}G_1(\eta) = \left(\frac{d^2}{d\eta^2}G_2(\eta)\right) + I\beta_v(g_2(\eta) - G_2(\eta)) - YG_2(\eta), \tag{17}$$

$$-\left(\frac{d}{d\eta}\theta(\eta)\right)G_1(\eta) = \frac{1}{Pr}\left(1 + \frac{4}{3}Rd\right)\left(\frac{d^2}{d\eta^2}\theta(\eta)\right) + Nb\frac{d}{d\eta}\theta(\eta)\frac{d}{d\eta}\phi(\eta) + Nt\left(\frac{d}{d\eta}\theta(\eta)\right)^2 + I\beta_t(\theta_p(\eta) - \theta(\eta)) + \frac{1}{Pr}\left(A\frac{d}{d\eta}G_1(\eta) + B\theta(\eta)\right), \tag{18}$$

$$-\left(\frac{\mathrm{d}}{\mathrm{d}\eta}\phi(\eta)\right)G_1(\eta) = \frac{1}{\mathrm{Sc}}\frac{\mathrm{d}^2}{\mathrm{d}\eta^2}\phi(\eta) + \frac{\mathrm{Nt}}{\mathrm{Nb}}\frac{1}{\mathrm{Sc}}\frac{\mathrm{d}^2}{\mathrm{d}\eta^2}\theta(\eta) + I\beta_c(\phi_\mathrm{p}(\eta) - \phi(\eta)), \tag{19}$$

$$-\Gamma((\theta_\mathrm{w}-1)\theta+1)^{n_1}\exp\left(\frac{-E}{(\theta_\mathrm{w}-1)\theta+1}\right)\phi(\eta) -\left(\frac{\mathrm{d}}{\mathrm{d}\eta}\chi(\eta)\right)G_1(\eta) + \frac{\mathrm{Pe}}{\mathrm{Lb}}\left[(\chi(\eta)+\chi_\mathrm{w})\frac{\mathrm{d}^2}{\mathrm{d}\eta^2}\phi(\eta) + \frac{\mathrm{d}}{\mathrm{d}\eta}\phi(\eta)\frac{\mathrm{d}}{\mathrm{d}\eta}\chi(\eta)\right] = \frac{1}{Lb}\frac{\mathrm{d}^2}{\mathrm{d}\eta^2}\chi(\eta). \tag{20}$$

2.4 Dusty phase

$$\left(\frac{\mathrm{d}}{\mathrm{d}\eta}g_1(\eta)\right)^2 - g_1(\eta)\frac{\mathrm{d}^2}{\mathrm{d}\eta^2}g_1(\eta) = \beta_\mathrm{v}\left(\frac{\mathrm{d}}{\mathrm{d}\eta}G_1(\eta) - \frac{\mathrm{d}}{\mathrm{d}\eta}g_1(\eta)\right), \tag{21}$$

$$\frac{\mathrm{d}}{\mathrm{d}\eta}g_1(\eta)g_2(\eta) - g_1(\eta)\frac{\mathrm{d}}{\mathrm{d}\eta}g_2(\eta) = \beta_\mathrm{v}(G_2(\eta) - g_2(\eta)), \tag{22}$$

$$-g_1(\eta)\frac{\mathrm{d}}{\mathrm{d}\eta}\theta_\mathrm{p}(\eta) = \gamma\beta_\mathrm{t}(\theta(\eta) - \theta_\mathrm{p}(\eta)), \tag{23}$$

$$-g_1(\eta)\frac{\mathrm{d}}{\mathrm{d}\eta}\phi_\mathrm{p}(\eta) = \gamma\beta_\mathrm{c}(\phi(\eta) - \phi_\mathrm{p}(\eta)), \tag{24}$$

where

$$I = \frac{mN}{\rho_\mathrm{f}}, \Upsilon = \frac{\upsilon_\mathrm{f}}{ak_1}, \beta_\mathrm{v} = \frac{1}{\tau_\mathrm{v}a}, \tau_\mathrm{v} = \frac{m}{K}, \beta_\mathrm{t} = \frac{1}{\tau_\mathrm{T}a}, \beta_\mathrm{c} = \frac{1}{\tau_\mathrm{C}a}, \gamma = \frac{c_\mathrm{p}}{c_\mathrm{m}}, \mathrm{Pe} = \frac{bW}{D_\mathrm{m}}, \mathrm{Lb} = \frac{\upsilon_\mathrm{f}}{D_\mathrm{m}}, \mathrm{Nb} = \frac{\tau D_\mathrm{B}(C_\mathrm{w}-C_\infty)}{\upsilon_\mathrm{f}}, \mathrm{Nt} = \frac{\tau D_\mathrm{T}(T_\mathrm{w}-T_\infty)}{T_\infty\upsilon_\mathrm{f}}, \mathrm{Sc} = \frac{\upsilon_\mathrm{f}}{D_\mathrm{B}}, \Gamma = \frac{\gamma_0^2}{a}, \theta_\mathrm{w} = \frac{T_\mathrm{w}}{T_\infty}, E = \frac{E_0}{k^*T_\infty}, \alpha = \frac{\Omega}{a}, \chi_\mathrm{w} = \frac{N_\infty}{N_\mathrm{w}-N_\infty}, \mathrm{Pr} = \frac{\mu_\mathrm{f}c_{\mathrm{p}_\mathrm{f}}}{k_\mathrm{f}}, \tag{25}$$

$$\left.\begin{aligned}&\frac{\mathrm{d}}{\mathrm{d}\eta}G_1(\eta) = 1, G_2(\eta) = 0, G_1(\eta) = 0, \theta(\eta) = 1,\\ &\phi(\eta) = 1, \chi(\eta) = 1, \quad \text{at } \eta = 0,\\ &\frac{\mathrm{d}}{\mathrm{d}\eta}G_1(\eta) \to 0, G_2(\eta) \to 0, \theta(\eta) \to 0, \phi(\eta) \to 0, \chi(\eta) \to 0,\\ &\frac{\mathrm{d}}{\mathrm{d}\eta}g_1(\eta) \to 0, g_2(\eta) \to 0, g_1(\eta) \to G_1(\eta), \theta_\mathrm{p}(\eta) \to 0, \phi_\mathrm{p}(\eta) \to 0, \quad \text{as } \eta \to \infty\end{aligned}\right\}. \tag{26}$$

Skin friction in three dimensions, heat transfer rate, mass transfer rate, and the local density number of motile microbes are provided by

$$C_{Ax} = \frac{2\tau_{wx}}{\rho_f u_\mathrm{w}^2}, C_{Ay} = \frac{2\tau_{wy}}{\rho_\mathrm{f}u_\mathrm{w}^2}, \mathrm{Nu} = \frac{xq_\mathrm{w}}{k_\mathrm{f}(T_\mathrm{w}-T_\infty)}, \mathrm{Sh} = \frac{xJ_\mathrm{w}}{D_\mathrm{B}(C_\mathrm{w}-C_\infty)}, N_x = \frac{xk_\mathrm{w}}{D_\mathrm{m}(N_\mathrm{w}-N_\infty)}, \tau_{wx} = \mu_\mathrm{f}\left(\frac{\partial v_1}{\partial z}\right)_{z=0}, \tau_{wx} = \mu_\mathrm{f}\left(\frac{\partial v_2}{\partial z}\right)_{z=0}, q_\mathrm{w} = -k_\mathrm{f}\left(\frac{\partial T}{\partial z}\right)_{z=0} + q_\mathrm{r}, J_\mathrm{w} = -D_\mathrm{B}\left(\frac{\partial C}{\partial z}\right)_{z=0}, k_\mathrm{w} = -D_\mathrm{m}\left(\frac{\partial N}{\partial z}\right)_{z=0}. \tag{27}$$

Using equations (15) and (27), we have

$$C_{Ax}\,\mathrm{Re}_x^{1/2}/2 = G_1''(0), C_{Ay}\,\mathrm{Re}_x^{1/2}/2 = G_2'(0), \mathrm{Nu}\,\mathrm{Re}_x^{-1/2} = -\left(1+\frac{4}{3}\mathrm{Rd}\right)\theta'(0), \mathrm{Sh}\,\mathrm{Re}_x^{-1/2} = -\phi'(0), N_x\,\mathrm{Re}_x^{-1/2} = -\chi'(0). \tag{28}$$

3 Methods of solution

The MATLAB bvp4c solver, along with the shooting technique, is employed to obtain numerical solutions to the coupled ordinary differential equations (ODEs) (16)–(24) subject to boundary conditions (26). The initial step in transforming the set of coupled nonlinear ODEs into a system of first-order differential equations is as follows:

$$\begin{aligned}&G_1(\eta) = f_1, \frac{\mathrm{d}}{\mathrm{d}\eta}G_1(\eta) = f_2, \frac{\mathrm{d}^2}{\mathrm{d}\eta^2}G_1(\eta) = f_3,\\ &\frac{\mathrm{d}^3}{\mathrm{d}\eta^3}G_1(\eta) = f_3', G_2(\eta) = f_4, \frac{\mathrm{d}}{\mathrm{d}\eta}G_2(\eta) = f_5,\\ &\frac{\mathrm{d}^2}{\mathrm{d}\eta^2}G_2(\eta) = f_5', \theta(\eta) = f_6, \frac{\mathrm{d}}{\mathrm{d}\eta}\theta(\eta) = f_7,\\ &\frac{\mathrm{d}^2}{\mathrm{d}\eta^2}\theta(\eta) = f_7', \phi(\eta) = f_8, \frac{\mathrm{d}}{\mathrm{d}\eta}\phi(\eta) = f_9,\\ &\frac{\mathrm{d}^2}{\mathrm{d}\eta^2}\phi(\eta) = f_9', \chi(\eta) = f_{10}, \frac{\mathrm{d}}{\mathrm{d}\eta}\chi(\eta) = f_{11},\\ &\frac{\mathrm{d}^2}{\mathrm{d}\eta^2}\chi(\eta) = f_{11}', g_1(\eta) = f_{12}, \frac{\mathrm{d}}{\mathrm{d}\eta}g_1(\eta) = f_{13},\\ &\frac{\mathrm{d}^2}{\mathrm{d}\eta^2}g_1(\eta) = f_{13}', g_2(\eta) = f_{14}, \frac{\mathrm{d}}{\mathrm{d}\eta}g_2(\eta) = f_{14}',\\ &\theta_\mathrm{p}(\eta) = f_{15}, \frac{\mathrm{d}}{\mathrm{d}\eta}\theta_\mathrm{p}(\eta) = f_{15}',\\ &\phi_\mathrm{p}(\eta) = f_{16}, \frac{\mathrm{d}}{\mathrm{d}\eta}\phi_\mathrm{p}(\eta) = f_{16}'.\end{aligned} \tag{29}$$

$$f_3' = (f_2)^2 - f_1f_3 - 2\alpha f_4 - I\beta_\mathrm{v}(f_{13} - f_2) + Yf_2, \tag{30}$$

$$f_5' = f_4f_2 - f_5f_1 + 2\alpha f_2 - I\beta_v(f_{14} - f_4) + \Upsilon f_4, \tag{31}$$

$$f_7' = \left[-f_7 f_1 - \mathrm{Nb} f_7 f_9 - \mathrm{Nt}(f_7)^2 - I\beta_t(f_{15} - f_6) - \frac{1}{\mathrm{Pr}}(Af_2 + Bf_6)\right] / \frac{1}{\mathrm{Pr}}\left(1 + \frac{4}{3}\mathrm{Rd}\right), \tag{32}$$

$$f_9' = \mathrm{Sc}\left(-f_9 f_1 - \frac{\mathrm{Nt}}{\mathrm{Nb}}\frac{1}{\mathrm{Sc}} f_7' - I\beta_c(f_{16} - f_8) + \Gamma((\theta_w - 1)f_6 + 1)^{n_1} \exp\left(\frac{-E}{(\theta_w - 1)f_6 + 1}\right) f_8\right), \tag{33}$$

$$f_{11}' = \mathrm{Lb}\left(-f_{11} f_1 + \frac{\mathrm{Pe}}{\mathrm{Lb}}[(f_{10} + \chi_w) f_9' + f_9 f_{11}]\right). \tag{34}$$

3.1 Dusty phase

$$f_{13}' = ((f_{13})^2 - \beta_v(f_2 - f_{13}))/f_{12}, \tag{35}$$

$$f_{14}' = (f_{13} f_{14} - \beta_v(f_4 - f_{14}))/f_{12}, \tag{36}$$

$$f_{15}' = (-\gamma\beta_t(f_6 - f_{15}))/f_{12}, \tag{37}$$

$$f_{16}' = (-\gamma\beta_c(f_8 - f_{16}))/f_{12}. \tag{38}$$

With boundary conditions

$$\begin{aligned} &f_2(0) = 1, f_4(0) = 0, f_1(0) = 0, f_6(0) = 1, \\ &f_8(0) = 1, f_{10}(0) = 1, \\ &f_2(\infty) \to 0, f_4(\infty) \to 0, f_6(\infty) \to 0, f_8(\infty) \to 0, \\ &f_{10}(\infty) \to 0, \\ &f_{12}(\infty) \to 0, f_{14}(\infty) \to 0, f_{12}(\infty) \to f_1(\infty), \\ &f_{15}(\infty) \to 0, f_{16}(\infty) \to 0. \end{aligned} \tag{39}$$

The variable step size $\eta_\infty = 0.001$ was used until the results asymptotically reached the tolerance limit of 10^{-8}.

4 Construction of ANN

ANN is a kind of architecture that interprets data in parallel by using numerous tiers of basic supplies that are intimately connected to one another and are referred to as cells. An ANN is a mathematical structure and a technologically sophisticated computer system that functions *via* the use of neuro-computing in order to efficiently manage data. Not only do ANNs have the ability to create networks of neurons, but they can also duplicate patterns. This model, which derives its cues from the human nervous system, has functional qualities that are indistinguishable from the characteristics of the genuine neuron. It comes from the human nervous system. Each and every one of the billions of sensory cells that are found in our skulls is used by the human brain, which is capable of doing enormous computations of any kind. For the purpose of remembering information, ANNs make use of weighted links, in contrast to genuine neurons, which keep their information in preservation. The calculation load that is connected with the generation of structural characteristics may be sped up and simplified with the help of this technique, which provides for the possibility of acceleration. The evident input and output levels are not the only levels that are present; there is also a hidden layer that contains components that are responsible for the information transformation. With this, the layer that is accountable for producing leads is able to use the output for decision-making, which is one of the mechanisms that constitutes ANNs. Artificial neurons have the astonishing capacity to easily recognize patterns and generate unique qualities that are difficult for both computers and humans to grasp. They are also able to extract important insights from incorrect data, which is a remarkable talent. In a broad sense, this may help to minimize the number of errors that take place [41].

Figure 2 shows the output of the jth hidden neuron.

$$y_j(x) = \sum_{i=1}^{1} W1_{ji} x_i + a_j. \tag{40}$$

where $W1_{ji}$ indicates the coupling weight between the two layers, x_i is the ith node's input layer, and a_j is the jth node's hidden layer.

The result showing the jth hidden node is shown below:

$$z_j(x) = \frac{1}{1 + e^{-y_j(x)}}. \tag{41}$$

This section considers the layer's kth output node

$$o_k(x) = \sum_{j=1}^{m} W2_{kj} z_j + b_k. \tag{42}$$

The weight $W2_{kj}$ of a connection between two nodes in the hidden layer and a node in the output layer indicates the strength of that connection. And you could see the word "bias" (or "b_k" for short) in the kth output layer node.

Multiple datasets were used to train, test, and verify the ANN algorithm. The model was trained using about 70% of the data, with the remaining 30% split evenly between validation and testing. Figure 3 shows the ANNs' layered architecture. The scenario HNF model's ANN training technique ran a regression analysis, and the results are shown in Figure 4.

According to Tables 1–4, the ANN algorithm outperformed the computational approaches in producing good

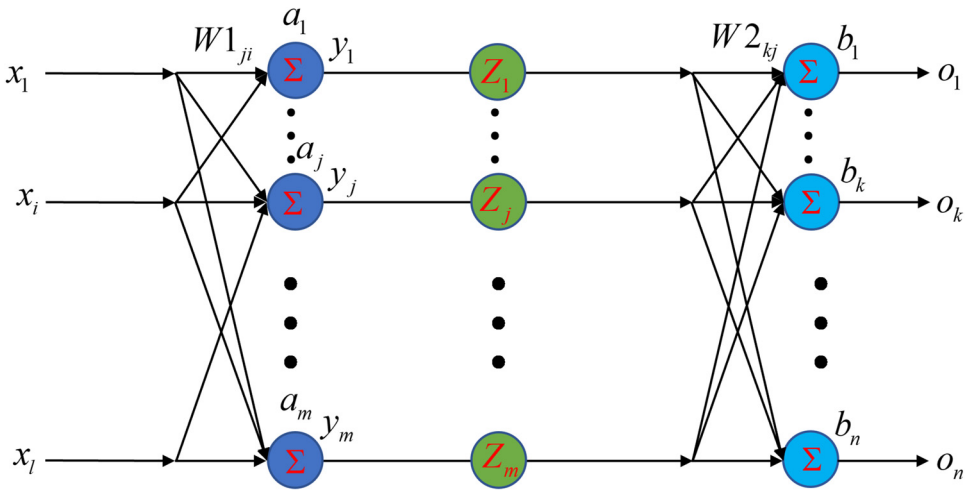

Figure 2: The back propagation of a neural network is shown schematically.

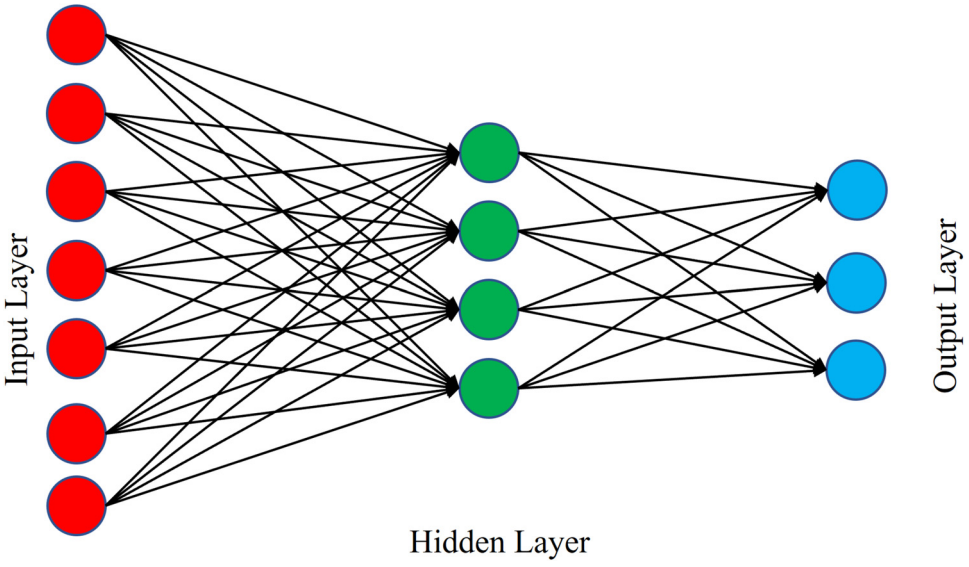

Figure 3: An ANN model with several layers is shown schematically.

outcomes. Previous research has shown that ANNs can reliably predict the rates of skin friction and heat transfer.

5 Findings and analysis

The purpose of this section is to show how the activation energy and Coriolis force affect the flow of a DF containing gyrotactic microbes over a three-dimensional surface. In this part, we look at the dusty and hybrid phases and how momentum and thermal characteristics are physically important. It also explores the key elements that affect the velocity of DNFs, including gyrotactic microorganisms. $(G_1'(\eta)\ \&\ g_1'(\eta))\ \&\ (G_2'(\eta)\ \&\ g_2'(\eta))$, temperature $(\theta(\eta)\ \&\ \theta_{\mathrm{p}}(\eta))$, concentration $(\phi(\eta)\ \&\ \phi_{\mathrm{p}}(\eta))$, motile microorganism $(\chi(\eta))$ skin friction $(C_{\mathrm{Ax}}\,\mathrm{Re}_x^{1/2})\ \&\ (C_{\mathrm{Ay}}\,\mathrm{Re}_x^{1/2})$, Nusselt number $(\mathrm{Nu}\,\mathrm{Re}_x^{-1/2})$, mass transfer rate $(\mathrm{Sh}\,\mathrm{Re}_x^{-1/2})$, and motile microorganism of local density number $(N_x\,\mathrm{Re}_x^{-1/2})$ are depicted, and a detailed discussion is held about them. The bvp4c with MATALB solver is used to solve the dimensional version of the flow, heat transport, concentration, and density equations of motile microorganisms under specific boundary conditions. The physical features of DF and DNF are compared over the three-dimensional

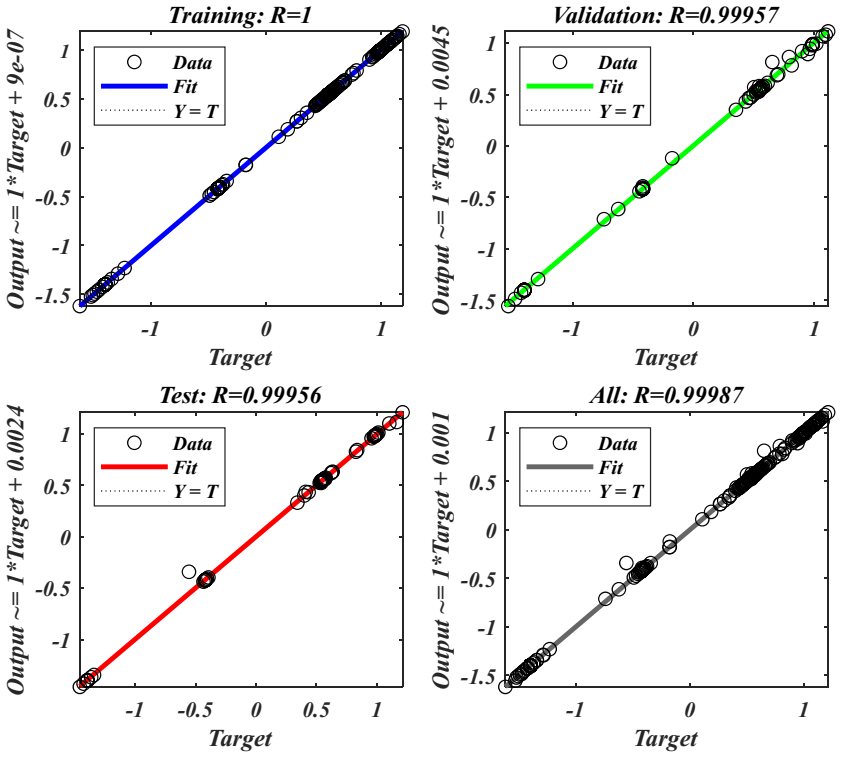

Figure 4: Statistical analysis with data from $(1/2C_f\,\mathrm{Re}_x^{1/2}X)$, $(\mathrm{Sh}\,\mathrm{Re}_x^{-1/2})$, and $(N_x\,\mathrm{Re}_x^{-1/2}X^{-1})$.

Table 1: ANN and numerical method (NM) values of $C_{Ax}\mathrm{Re}_x^{1/2}$ and $C_{Ay}\,\mathrm{Re}_x^{1/2}$

β_v	Y	l	α	$C_{Ax}\mathrm{Re}_x^{1/2}$			$C_{Ay}\mathrm{Re}_x^{1/2}$		
				NM	ANN	Error	NM	ANN	Error
0.2	0.1	2	0.5	−1.28500	−1.29336	8.35×10^{-3}	−0.44674	−0.43955	7.19×10^{-3}
0.4	0.1	2	0.5	−1.36623	−1.36676	5.26×10^{-4}	−0.42593	−0.42535	5.84×10^{-4}
0.6	0.1	2	0.5	−1.42569	−1.42570	1.51×10^{-5}	−0.41424	−0.41442	1.89×10^{-4}
0.8	0.1	2	0.5	−1.47085	−1.47085	9.47×10^{-7}	−0.40650	−0.40666	1.61×10^{-4}
1	0.1	2	0.5	−1.50628	−1.50625	2.69×10^{-5}	−0.40080	−0.40067	1.33×10^{-4}
0.5	0.1	2	0.5	−1.39813	−1.39812	1.01×10^{-5}	−0.41939	−0.41943	4.64×10^{-5}
0.5	0.2	2	0.5	−1.42935	−1.42975	3.99×10^{-4}	−0.40695	−0.40672	2.28×10^{-4}
0.5	0.3	2	0.5	−1.46033	−1.46048	1.55×10^{-4}	−0.39539	−0.39503	3.64×10^{-4}
0.5	0.4	2	0.5	−1.49102	−1.49090	1.15×10^{-4}	−0.38464	−0.38440	2.42×10^{-4}
0.5	0.5	2	0.5	−1.52140	−1.52150	1.00×10^{-4}	−0.37462	−0.37483	2.09×10^{-4}
0.5	0.1	0.5	0.5	−1.22997	−1.22984	1.29×10^{-4}	−0.47260	−0.47243	1.67×10^{-4}
0.5	0.1	1	0.5	−1.28733	−1.28756	2.22×10^{-4}	−0.45330	−0.45369	3.85×10^{-4}
0.5	0.1	1.5	0.5	−1.34339	−1.34500	1.60×10^{-3}	−0.43560	−0.43597	3.73×10^{-4}
0.5	0.1	2.5	0.5	−1.45155	−1.45153	1.73×10^{-5}	−0.40453	−0.40480	2.67×10^{-4}
0.5	0.1	2	0.2	−1.34199	−1.34179	1.95×10^{-4}	−0.17827	−0.17845	1.86×10^{-4}
0.5	0.1	2	0.4	−1.37593	−1.37680	8.69×10^{-4}	−0.34343	−0.34231	1.12×10^{-3}
0.5	0.1	2	0.6	−1.42255	−1.42281	2.52×10^{-4}	−0.49097	−0.49034	6.36×10^{-4}
0.5	0.1	2	0.8	−1.47550	−1.48506	9.56×10^{-3}	−0.62229	−0.61223	1.01×10^{-2}
0.5	0.1	2	1	−1.53115	−1.55502	2.39×10^{-2}	−0.74025	−0.71106	2.92×10^{-2}

Table 2: ANN and NM values of $\mathrm{NuRe}_x^{-1/2}$

Rd	A	B	β_t	Γ	Nt	Nb	$\mathrm{NuRe}_x^{-1/2}$		
							NM	ANN	Error
0.5	1	1	0.5	1	0.2	0.2	1.123029	1.122525	5.04×10^{-4}
0.7	1	1	0.5	1	0.2	0.2	1.063285	1.064012	7.27×10^{-4}
0.9	1	1	0.5	1	0.2	0.2	1.010646	1.011047	4.00×10^{-4}
1.1	1	1	0.5	1	0.2	0.2	0.96383	0.963699	1.30×10^{-4}
1.3	1	1	0.5	1	0.2	0.2	0.921836	0.921834	2.46×10^{-6}
1	0.2	1	0.5	1	0.2	0.2	1.111102	1.110997	1.05×10^{-4}
1	0.3	1	0.5	1	0.2	0.2	1.095564	1.095749	1.86×10^{-4}
1	0.4	1	0.5	1	0.2	0.2	1.080018	1.080167	1.49×10^{-4}
1	0.5	1	0.5	1	0.2	0.2	1.064465	1.064394	7.04×10^{-5}
1	0.6	1	0.5	1	0.2	0.2	1.048903	1.048562	3.42×10^{-4}
1	1	0.2	0.5	1	0.2	0.2	1.113345	1.113623	2.78×10^{-4}
1	1	0.3	0.5	1	0.2	0.2	1.098184	1.098261	7.66×10^{-5}
1	1	0.4	0.5	1	0.2	0.2	1.082842	1.082799	4.35×10^{-5}
1	1	0.5	0.5	1	0.2	0.2	1.067312	1.067215	9.68×10^{-5}
1	1	0.6	0.5	1	0.2	0.2	1.051587	1.051489	9.86×10^{-5}
1	1	1	0.2	1	0.2	0.2	0.651795	0.815917	1.64×10^{-1}
1	1	1	0.3	1	0.2	0.2	0.790207	0.864505	7.43×10^{-2}
1	1	1	0.4	1	0.2	0.2	0.898218	0.921206	2.30×10^{-2}
1	1	1	0.5	1	0.2	0.2	0.986578	0.986675	9.64×10^{-5}
1	1	1	0.6	1	0.2	0.2	1.061072	1.061072	4.66×10^{-7}
1	1	1	0.5	0.1	0.2	0.2	1.213823	1.211967	1.86×10^{-3}
1	1	1	0.5	0.2	0.2	0.2	1.184912	1.18449	4.22×10^{-4}
1	1	1	0.5	0.3	0.2	0.2	1.156972	1.157182	2.11×10^{-4}
1	1	1	0.5	0.4	0.2	0.2	1.129979	1.130291	3.12×10^{-4}
1	1	1	0.5	0.5	0.2	0.2	1.103912	1.104025	1.14×10^{-4}
1	1	1	0.5	1	0.05	0.2	1.083454	1.083309	1.45×10^{-4}
1	1	1	0.5	1	0.1	0.2	1.050012	1.050340	3.28×10^{-4}
1	1	1	0.5	1	0.15	0.2	1.017731	1.017488	2.43×10^{-4}
1	1	1	0.5	1	0.2	0.2	0.986578	0.986675	9.64×10^{-5}
1	1	1	0.5	1	0.25	0.2	0.956518	0.959041	2.52×10^{-3}
1	1	1	0.5	1	0.2	0.05	1.139136	1.139144	8.50×10^{-6}
1	1	1	0.5	1	0.2	0.1	1.086488	1.086492	4.29×10^{-6}
1	1	1	0.5	1	0.2	0.15	1.035641	1.035751	1.10×10^{-4}
1	1	1	0.5	1	0.2	0.2	0.986578	0.986675	9.64×10^{-5}
1	1	1	0.5	1	0.2	0.25	0.939281	0.939489	2.08×10^{-4}

figure sheet using rotational parameter (α) as solid and dotted lines, respectively. Table 5 shows that there is a significant level of consensus in the comparative study, hence the numerical simulation results are dependable.

5.1 Effect of fluid–particle interaction (β_v)

Figure 5(a–d) depicts how the fluid–particle interaction parameter (β_v) affected the velocities ($G_1'(\eta)$ & $g_1'(\eta)$), temperature ($\theta(\eta)$ & $\theta_p(\eta)$), concentration ($\phi(\eta)$ & $\phi_p(\eta)$), and motile microorganism ($\chi(\eta)$) profiles in the case of ($\alpha = 0.5$) and ($\alpha = 1$), respectively. Figure 5(a) explores the effect of changes in (β_v) on ($G_1'(\eta)$)(DF) and $g_1'(\eta)$ (DNF) in the case of rotational parameter ($\alpha = 0.5$) and ($\alpha = 1$). Findings show that $G_1'(\eta)$ decreases with increasing (β_v) values and increases with increasing $g_1'(\eta)$. In terms of physical effects, a larger value of (β_v) reduces the particle phase relaxation time and increases the drag force acting on the interacting fluid. The effect of (β_v) on the temperature profile ($\theta(\eta)$ & $\theta_p(\eta)$) is illustrated in Figure 5(b), and it is observed that increasing (β_v) causes ($\theta(\eta)$ & $\theta_p(\eta)$) to enlarge. It is observed that $\theta(\eta)$ has stronger effects than the $\theta_p(\eta)$. Moreover ($\alpha = 1$) has more effective than ($\alpha = 0.5$). In Figure 5(c), the effect of (β_v) on concentration ($\phi(\eta)$ & $\phi_p(\eta)$) is presented. A closer inspection at the graph reveals that when (β_v) increases, ($\phi(\eta)$) and ($\phi_p(\eta)$) increase. Figure 5(d) illustrates how the

Table 3: ANN and NM values of $\mathrm{ShRe}_x^{-1/2}$

Sc	γ	θ_w	E	β_c	n1	$\mathrm{ShRe}_x^{-1/2}$		
						NM	ANN	Error
0.2	0.5	1.5	1	0.5	0.5	−0.556680	−0.340330	2.16×10^{-1}
0.4	0.5	1.5	1	0.5	0.5	−0.176150	-0.119010	5.71×10^{-2}
0.6	0.5	1.5	1	0.5	0.5	0.109308	0.109317	9.25×10^{-6}
0.8	0.5	1.5	1	0.5	0.5	0.341719	0.332926	8.79×10^{-3}
1	0.5	1.5	1	0.5	0.5	0.540186	0.540122	6.44×10^{-5}
1	0.2	1.5	1	0.5	0.5	0.399204	0.402061	2.86×10^{-3}
1	0.4	1.5	1	0.5	0.5	0.495065	0.495306	2.40×10^{-4}
1	0.6	1.5	1	0.5	0.5	0.583659	0.583609	5.02×10^{-5}
1	0.8	1.5	1	0.5	0.5	0.666208	0.666407	1.99×10^{-4}
1	1	1.5	1	0.5	0.5	0.743640	0.743583	5.72×10^{-5}
1	0.5	0.5	1	0.5	0.5	0.425713	0.425475	2.38×10^{-4}
1	0.5	1	1	0.5	0.5	0.484723	0.485345	6.22×10^{-4}
1	0.5	1.5	1	0.5	0.5	0.540186	0.540122	6.44×10^{-5}
1	0.5	2	1	0.5	0.5	0.590057	0.589959	9.73×10^{-5}
1	0.5	2.5	1	0.5	0.5	0.634937	0.635058	1.21×10^{-4}
1	0.5	1.5	0.5	0.5	0.5	0.645172	0.644991	1.82×10^{-4}
1	0.5	1.5	0.6	0.5	0.5	0.621603	0.621791	1.88×10^{-4}
1	0.5	1.5	0.7	0.5	0.5	0.599363	0.599529	1.66×10^{-4}
1	0.5	1.5	0.8	0.5	0.5	0.578410	0.578376	3.46×10^{-5}
1	0.5	1.5	0.9	0.5	0.5	0.558700	0.558511	1.90×10^{-4}
1	0.5	1.5	1	0.2	0.5	0.354393	0.354404	1.13×10^{-5}
1	0.5	1.5	1	0.4	0.5	0.495255	0.495489	2.34×10^{-4}
1	0.5	1.5	1	0.6	0.5	0.575585	0.575873	2.88×10^{-4}
1	0.5	1.5	1	0.8	0.5	0.627909	0.629297	1.39×10^{-3}
1	0.5	1.5	1	1	0.5	0.664793	0.664781	1.27×10^{-5}

Table 4: ANN and NM values of $\mathrm{N_xRe}_x^{-1/2}$

Lb	Pe	χ_w	$\mathrm{N_xRe}_x^{-1/2}$		
			NM	ANN	Error
0.1	0.1	0.5	0.186948	0.186172	7.76×10^{-4}
0.3	0.1	0.5	0.266109	0.267456	1.35×10^{-3}
0.5	0.1	0.5	0.351812	0.351661	1.50×10^{-4}
0.7	0.1	0.5	0.435993	0.435221	7.72×10^{-4}
0.9	0.1	0.5	0.515392	0.515152	2.41×10^{-4}
1	0.2	0.5	0.621191	0.619026	2.16×10^{-3}
1	0.3	0.5	0.689628	0.687994	1.63×10^{-3}
1	0.4	0.5	0.758395	0.758442	4.65×10^{-5}
1	0.5	0.5	0.827481	0.828669	1.19×10^{-3}
1	0.6	0.5	0.896875	0.896838	3.75×10^{-5}
1	0.1	0.2	0.539954	0.539980	2.61×10^{-5}
1	0.1	0.3	0.544334	0.544349	1.46×10^{-5}
1	0.1	0.4	0.548715	0.548725	1.03×10^{-5}
1	0.1	0.5	0.553095	0.553127	3.23×10^{-5}
1	0.1	0.6	0.557475	0.557576	1.01×10^{-4}

(β_v) influences motile microorganism ($\chi(\eta)$) changes in the case of rotational parameter (α = 0.5) and (α = 1), respectively. It is observed that ($\chi(\eta)$) increases with the increase in (β_v).

Table 5: Comparison of $-\theta'(0)$ for various values of Pr with previous work

Pr	Rehman *et al.* [42]	Ali *et al.* [43]	Present
1.0	1.00000	1.0000	1.00000
3.0	1.92375	1.9236	1.92375
10	3.72061	3.7207	3.72061
100	12.29404	12.294	12.29404

5.2 Effect of porosity (Y)

Figure 6(a–d) describes variations in the velocities ($G_1'(\eta)$ & $g_1'(\eta)$), temperature ($\theta(\eta)$ & $\theta_p(\eta)$), concentration ($\phi(\eta)$ & $\phi_p(\eta)$), and motile microorganism ($\chi(\eta)$) profiles influenced by the porosity parameter (Y). The velocity profile of a system is affected by the permeability parameter (Y), as seen in Figure 6(a). By increasing the values of the permeability parameter (Y), it is found that the ($G_1'(\eta)$ & $g_1'(\eta)$) profiles decline in both the cases of (α = 0.5) and (α = 1). The pore size of a material physically decreases as its permeability increases. When fluid flow slows down, fluid velocity also drops. Figure 6(b) portrays how the ($\theta(\eta)$ & $\theta_p(\eta)$) gets impacted for the variations in permeability parameter (Y) in (α = 0.5) and (α = 1). It is observed that the energy profiles for both the dusty and nanofluid cases ($\theta(\eta)$ & $\theta_p(\eta)$) increase with higher values of the (Y). As a result of low velocity, heat dissipation is restricted, which leads to an increase in temperature since the porous medium is able to maintain thermal energy. The concentration profile ($\phi(\eta)$ & $\phi_p(\eta)$) reveals a similar nature for the permeability parameter (Y) in Figure 6(c). Figure 6(d) illustrates how the (Y) influences the motile microorganism ($\chi(\eta)$) changes in the case of rotational parameter (α = 0.5) and (α = 1), respectively. It is observed that ($\chi(\eta)$) increases with the increase in the (Y). A higher permeability causes mass diffusion to be slowed down, which results in the accumulation of nanoparticles and an increase in concentration at the surface.

5.3 Effect of mass concentration of dust particles (I)

The impact of (I) on ($G_1'(\eta)$ & $g_1'(\eta)$), ($\theta(\eta)$ & $\theta_p(\eta)$), and ($\phi(\eta)$ & $\phi_p(\eta)$) profiles in the case of (α = 0.5) and (α = 1) are represented in Figure 7(a–c). Figure 7(a) explores the changes in mass concentration of dust particles (I) on transverse velocity ($G_1'(\eta)$ & $g_1'(\eta)$). It is detected that the transverse fluid velocity and transverse DF velocity enlargement by improving the (I). A physical explanation for

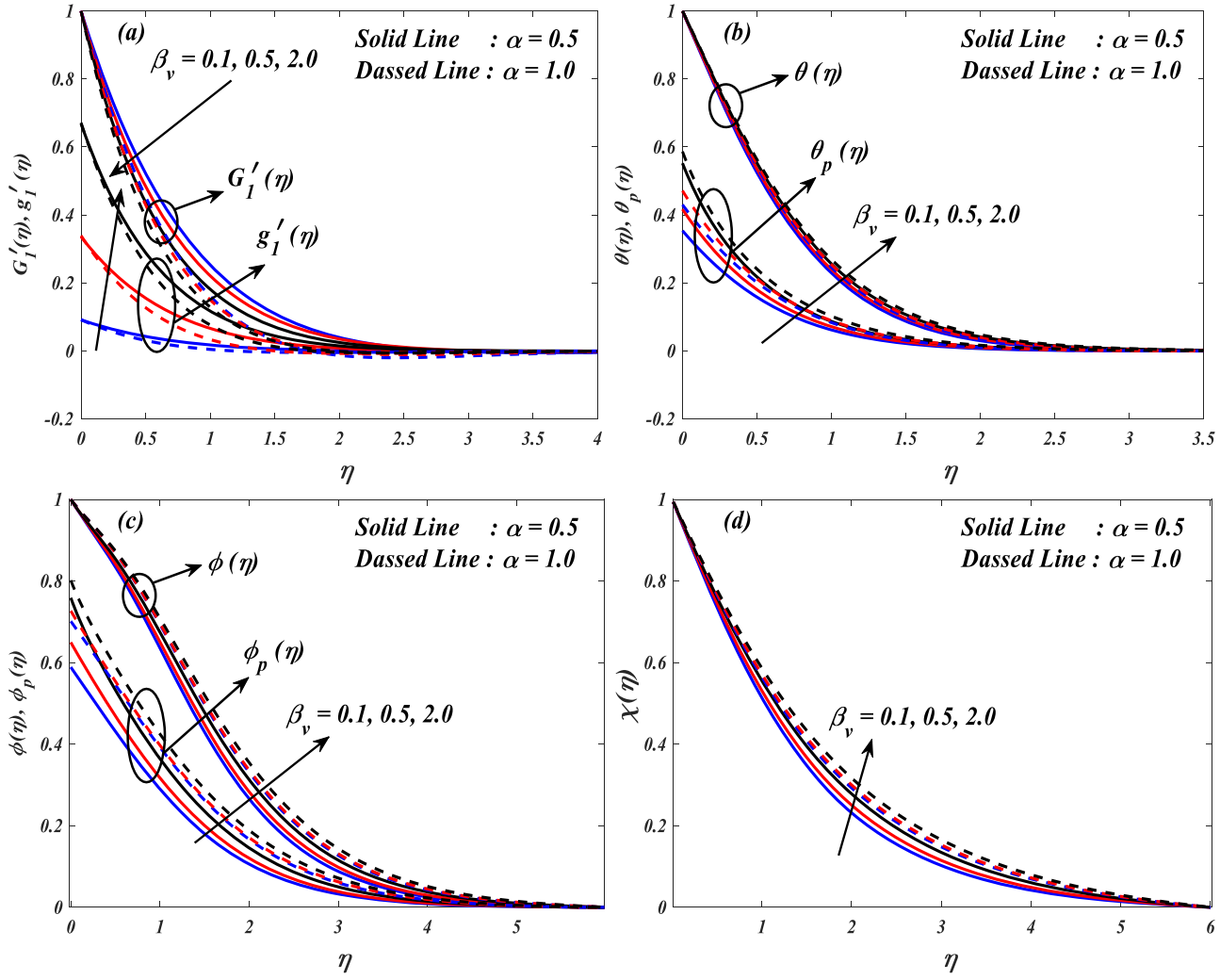

Figure 5: Influence of β_v on (a) $G_1'(\eta)$ & $g_1'(\eta)$, (b) $\theta(\eta)$ & $\theta_p(\eta)$, (c) $\phi(\eta)$ & $\phi_p(\eta)$, and (d) $\chi(\eta)$.

why certain fluids may move at higher velocities than others is that adding more dust to a mixture lowers the drag force a given fluid experiences. Figure 7(b) illustrates how the mass concentration of dust particles (I) affects the temperature's profile ($\theta(\eta)$ & $\theta_p(\eta)$) in a system. It is observed that both temperature profiles ($\theta(\eta)$ & $\theta_p(\eta)$) decrease as the values of (I) increase for (α = 0.5) and (α = 1). Due to dust's ability to absorb heat and promote energy dissipation, a lower system temperature is achieved with a higher concentration of dust, diminishing the thermal profile. Figure 7(c) demonstrates the influence of (I) on concentration ($\phi(\eta)$ & $\phi_p(\eta)$) variations. As the values of (I) increase, the concentration ($\phi(\eta)$ & $\phi_p(\eta)$) decreases, as seen in this diagram. Enhanced particle interactions promote dispersion and prevent aggregation near the surface, because the concentration profile decreases as the value of I increases. This is because the concentration profile lowers.

5.4 Effect of thermophoresis (Nt)

The impact of the (Nt) on ($\theta(\eta)$ & $\theta_p(\eta)$) and ($\phi(\eta)$ & $\phi_p(\eta)$) profiles in the case of (α = 0.5) and (α = 1) are represented in Figure 8(a and b). Figure 8(a) describes how the ($\theta(\eta)$ & $\theta_p(\eta)$) influenced the fluid and dusty phases to the deviations in (Nt). It is detected that ($\theta(\eta)$ & $\theta_p(\eta)$) increases with the increase in (Nt). This happens because thermophoresis exposes a bigger thermal boundary layer and pulls huge thermally conductive nanoparticles further into the fluid. The variations that can be found in a

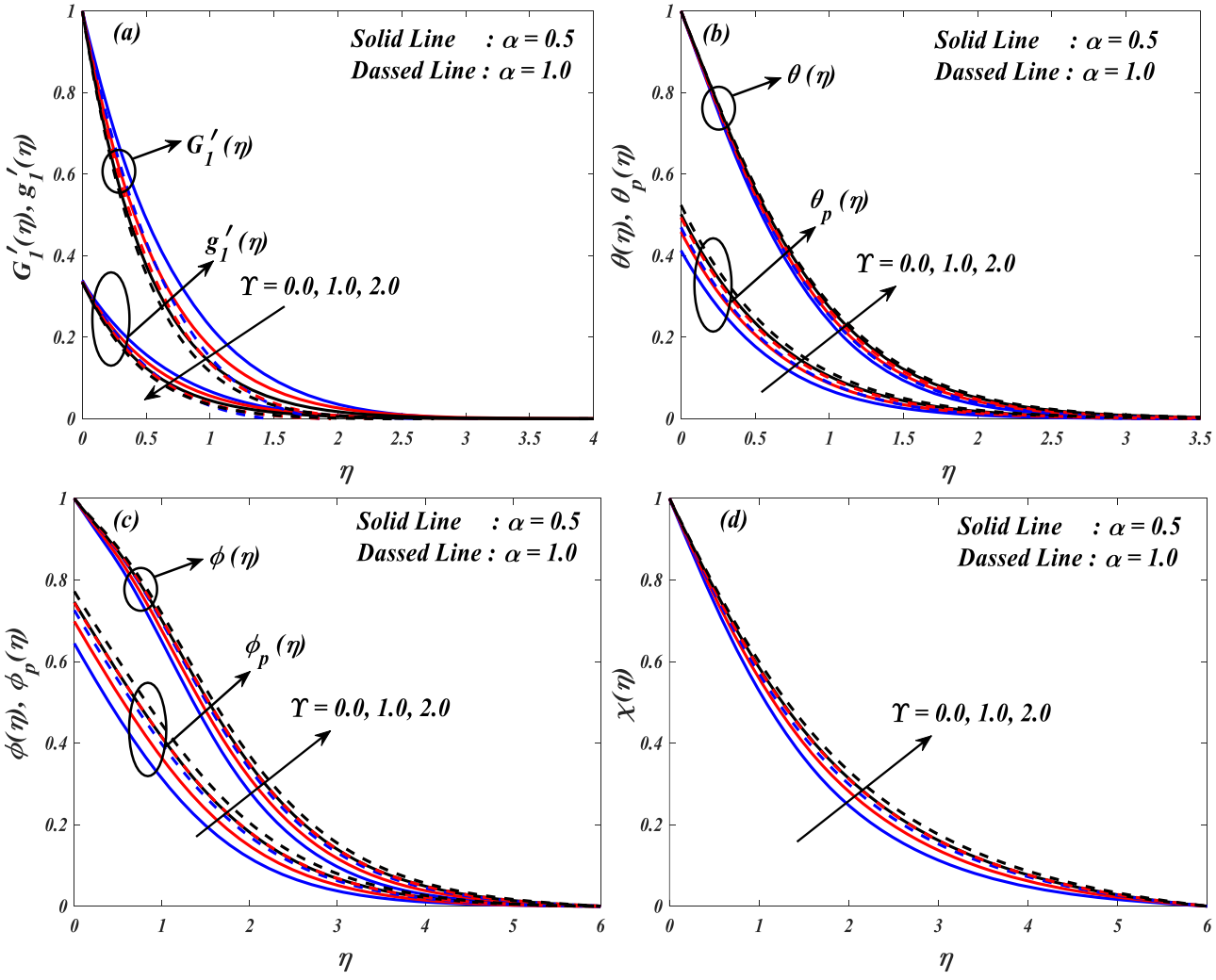

Figure 6: Influence of Y on (a) $G_1'(\eta)$&$g_1'(\eta)$, (b) $\theta(\eta)$&$\theta_p(\eta)$, (c) $\phi(\eta)$&$\phi_p(\eta)$, and (d) $\chi(\eta)$.

concentration profile ($\phi(\eta)$ & $\phi_p(\eta)$) according to a number of thermophoresis values (Nt) can be seen in Figure 8(b). The dusty stale air ($\phi_p(\eta)$) and fluid ($\phi(\eta)$) increased for higher values of (Nt). As the fluid concentration increases, its effects are limited to a slight enhancement of the wall slope in the concentration profiles. It is seen that the concentration of both the fluid and dusty phases increases in tandem with the increase in *Nt*. The effect, on the other hand, is most strongly detected close to the surface, which is where the concentration gradient becomes a little high. This occurs as a result of thermophoresis, which repositions particles within the fluid by driving them away from regions that are significantly heated.

5.5 Effect of Brownian motion (Nb)

The Brownian motion parameter's (Nb) impact on the temperature ($\theta(\eta)$ & $\theta_p(\eta)$) and concentration ($\phi(\eta)$ & $\phi_p(\eta)$) profiles in the case of (α = 0.5) and (α = 1) are presented in Figure 9(a and b). The impact of the ($\theta(\eta)$ & $\theta_p(\eta)$) on the two phases as well as the variations in the parameter (Nb) is shown in Figure 9(a). It has been understood that ($\theta(\eta)$ & $\theta_p(\eta)$) augmentations upsurge (Nb). As a result of an increase in the Brownian motion parameter, which raises the temperature and increases the kinetic energy, nanoparticles come in contact with the basic liquid particles. The variations that can be found in a ($\phi(\eta)$ & $\phi_p(\eta)$)

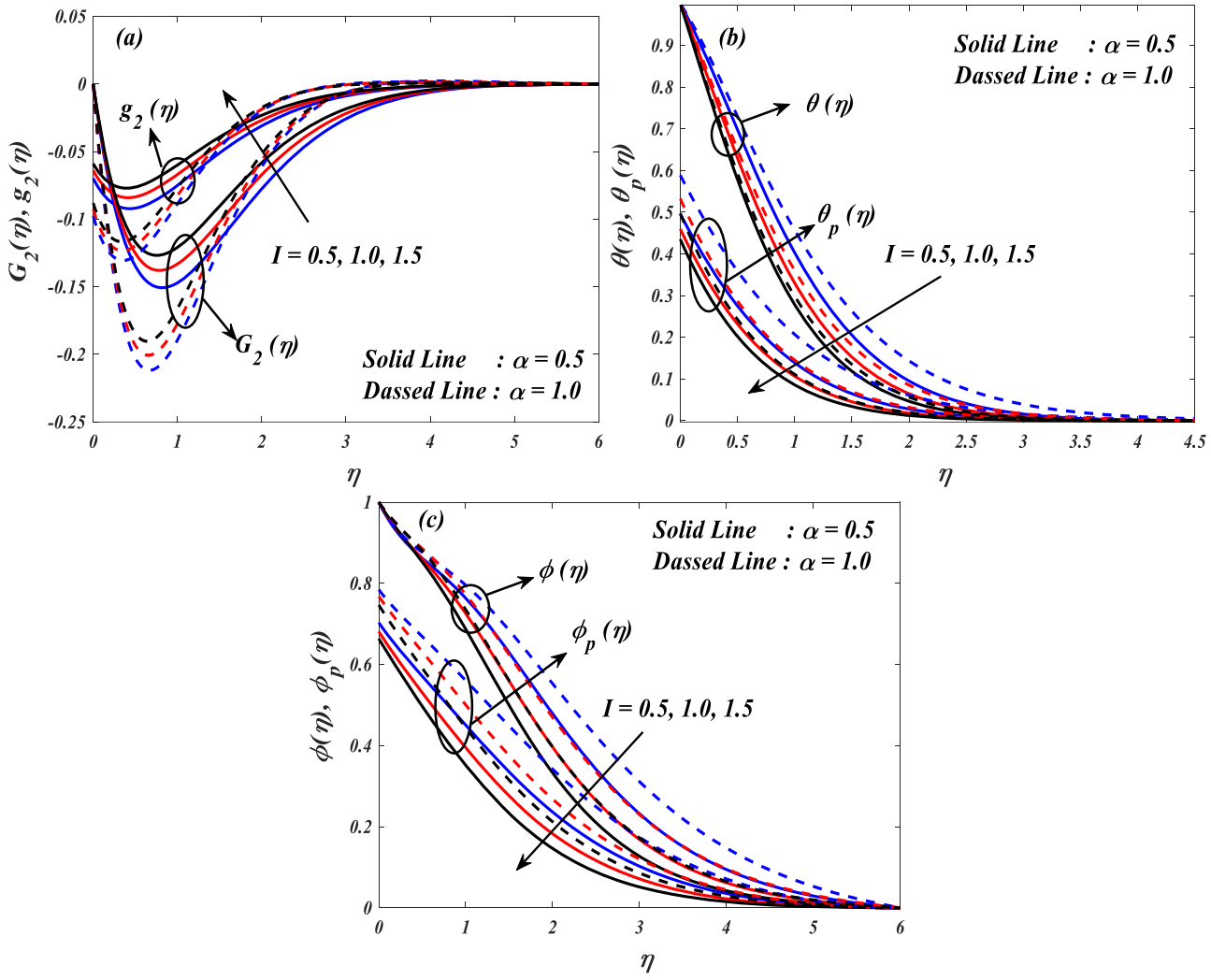

Figure 7: Influence of I on (a) $G_1'(\eta)$ & $g_1'(\eta)$, (b) $\theta(\eta)$ & $\theta_p(\eta)$, and (c) $\phi(\eta)$ & $\phi_p(\eta)$.

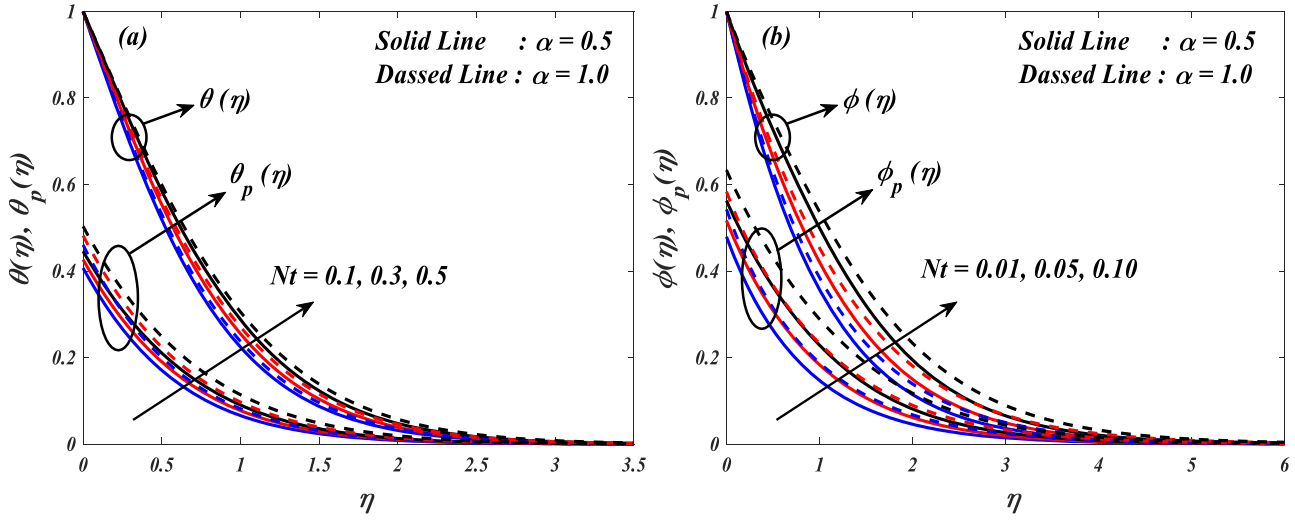

Figure 8: Influence of Nt on (a) $\theta(\eta)$ & $\theta_p(\eta)$ and (b) $\phi(\eta)$ & $\phi_p(\eta)$.

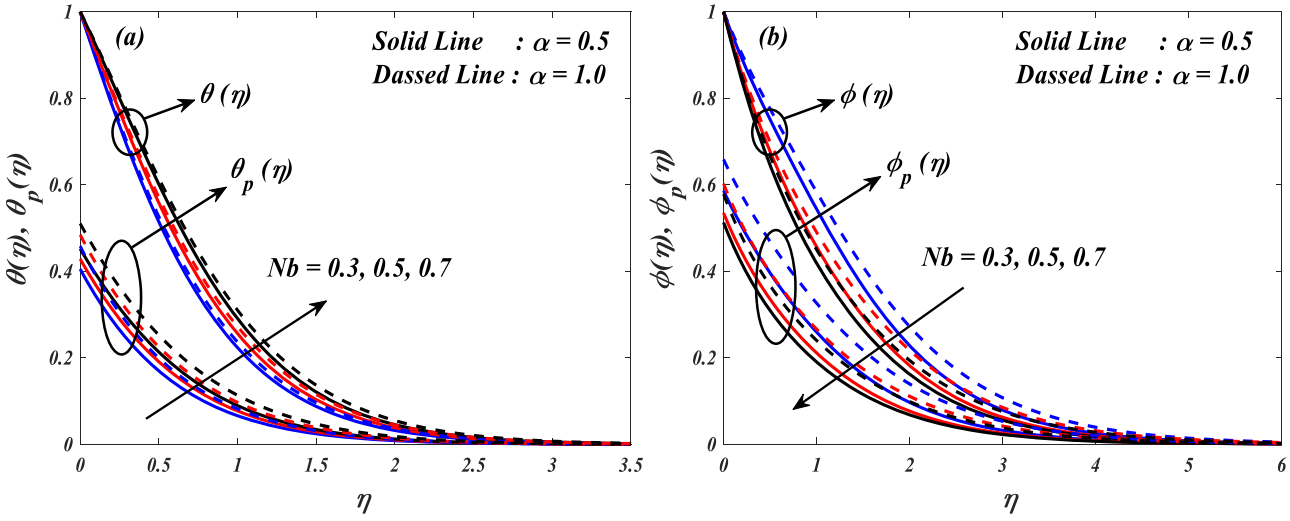

Figure 9: Influence of Nb on (a) $\theta(\eta)$ & $\theta_p(\eta)$ and (b) $\phi(\eta)$ & $\phi_p(\eta)$.

for multiple values of the (Nb) is illustrated in Figure 9(b). The dusty ($\phi_p(\eta)$) and fluid nanofluid ($\phi(\eta)$) increase for higher values of (Nb). When the Brownian motion of the fluid particles is increased, the random movement of the fluid particles improves physically. This results in an increase in the creation of heat, which in turn raises the temperature of the fluid.

5.6 Effect of specific heat ratio (γ)

Figure 10(a and b) explores the effect of changes in (γ) on ($\theta(\eta)$ & $\theta_p(\eta)$) and ($\phi(\eta)$ & $\phi_p(\eta)$) in the case of (α = 0.5) and (α = 1). Figure 10(a) demonstrates the influence on the temperature profile ($\theta(\eta)$ & $\theta_p(\eta)$) is impacted with the deviations in specific heat ratio parameter (γ). It is detected that ($\theta(\eta)$ & $\theta_p(\eta)$) increases with the increase in (γ). When the specific heat ratio parameter (γ) is increased, the fluid's capacity to store thermal energy is enhanced, which ultimately results in an increase in temperature. This arises as a consequence of the fact that a greater specific heat permits the fluid to absorb more heat before experiencing a change in temperature, which ultimately results in a thermal barrier layer that is thicker.

The same nature is observed for the concentration profile ($\phi(\eta)$ & $\phi_p(\eta)$), which is depicted in Figure 10(b). A higher value of γ results in an increase in the energy absorption

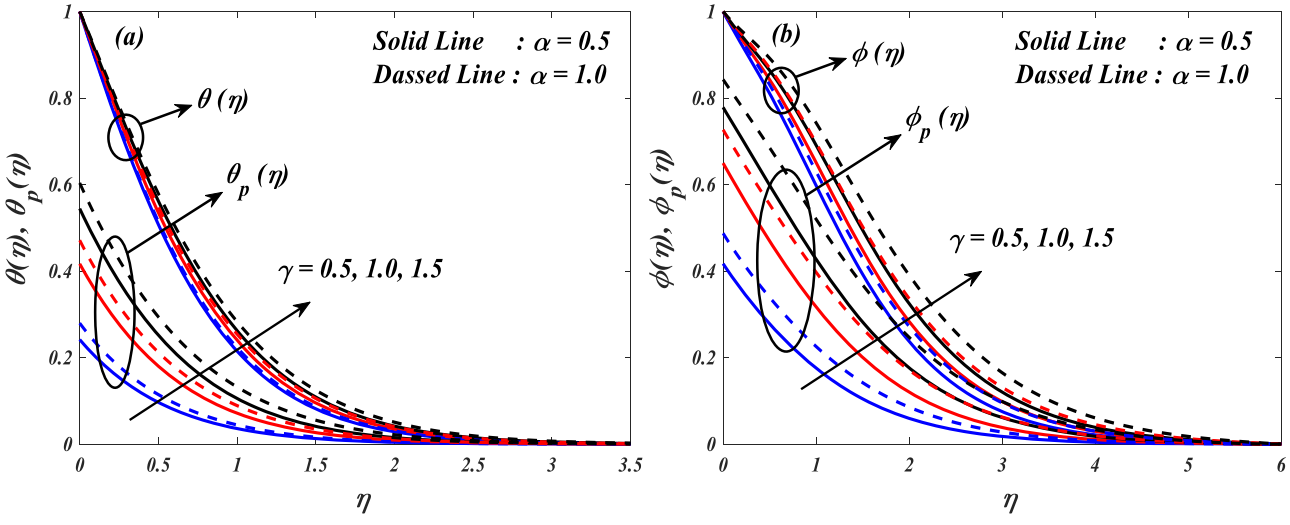

Figure 10: Influence of γ on (a) $\theta(\eta)$ & $\theta_p(\eta)$ and (b) $\phi(\eta)$ & $\phi_p(\eta)$.

capacity of the fluid, which in turn has an effect on the diffusion process. Heat causes improved mixing and dispersion throughout the system, thereby resulting in a larger concentration of nanoparticles within the fluid phase.

5.7 Effects of radiation (Rd) and accumulation (*A*)&(*B*)

Figure 11 demonstrates the influence of the radiation parameter (Rd) on the temperature profiles of the fluid and dusty phases. The graph presented here indicates that the temperature ($\theta(\eta)$ & $\theta_p(\eta)$) increases with the increase in the values of (Rd). In a physical sense, there is a correlation

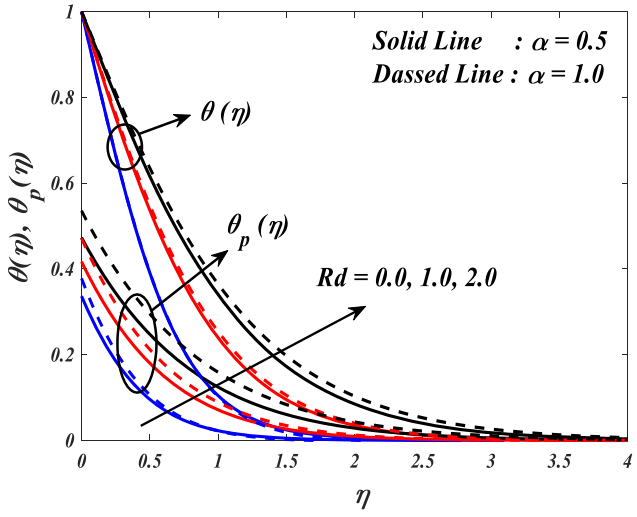

Figure 11: Influence of Rd on $\theta(\eta)$ & $\theta_p(\eta)$.

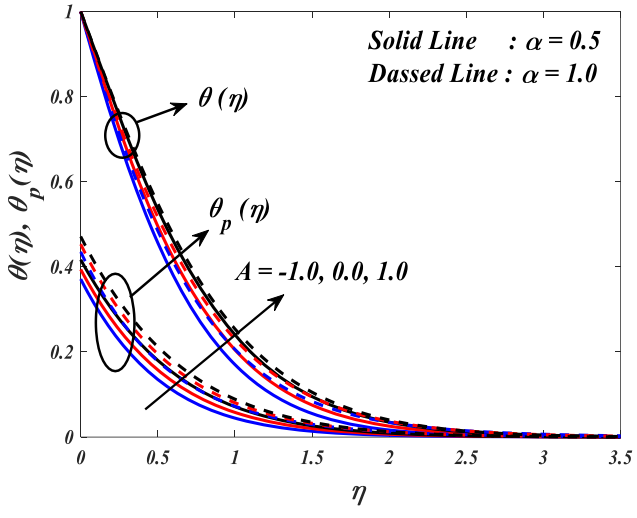

Figure 12: Influence of A on $\theta(\eta)$ & $\theta_p(\eta)$.

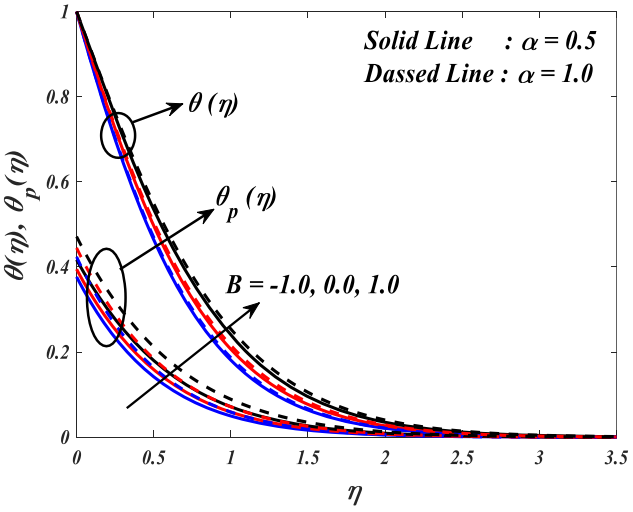

Figure 13: Influence of B on $\theta(\eta)$ & $\theta_p(\eta)$.

between higher temperatures and thicker thermal barrier layers and larger thermal radiation parameters. Figures 12 and 13 illustrate how (*A*)&(*B*) affect the temperature ($\theta(\eta)$ & $\theta_p(\eta)$). The wider dispersion of temperatures was shown to be an effect of the accumulation of (A) and (B) values. The main cause of warmth in the flow is an irritation in the levels of irregular heat parameters. The result was that, when the values of (A) and (B) increased, the fluid's temperature increased. In a physical sense, the increased heat energy causes a disruption in the thermal equilibrium, which in turn leads to an increase in molecular agitation and an increase in ambient temperature throughout the fluid.

5.8 Effect of fluid–particle interaction (β_t)

Figure 14 displays the variations in the temperature profile ($\theta(\eta)$ & $\theta_p(\eta)$) with the number of different fluid–particle interaction parameter for temperature values (β_t). Fluid temperature ($\theta(\eta)$) decreases while DNF ($\theta_p(\eta)$) increases at higher levels of (β_t). There is a loss of both kinetic and thermal energy for the micro fluid whenever it comes in contact with dust particles. It is a loss of a bodily nature.

5.9 Effect of fluid–particle interaction (*E*)

Figure 15 demonstrates how the activation energy parameter (E) affects the concentration profile ($\phi(\eta)$ & $\phi_p(\eta)$) in the case of (α = 0.5) and (α = 1) in the system. It is distinguished that the ($\phi(\eta)$ & $\phi_p(\eta)$) profiles efficiency increases with the increasing values of the activation energy

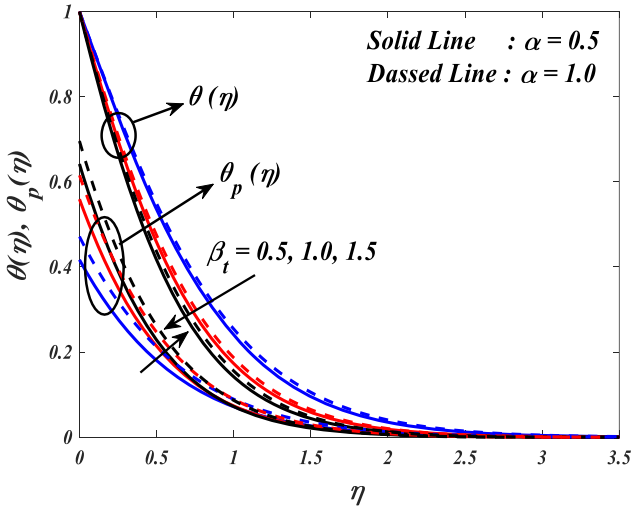

Figure 14: Influence of β_t for temperature on $\theta(\eta)$ & $\theta_p(\eta)$.

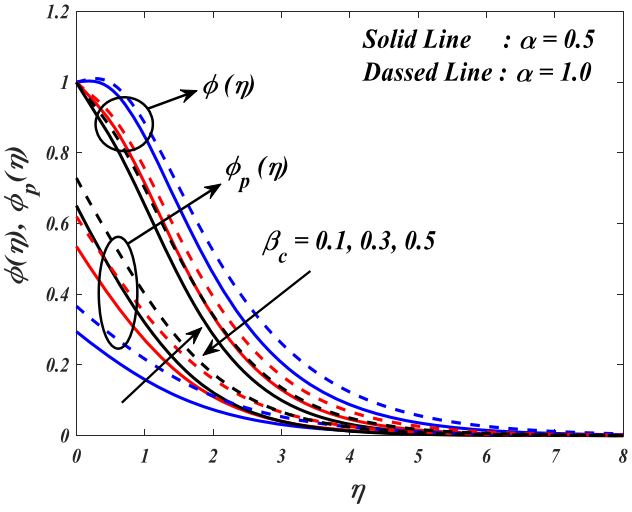

Figure 17: Influence of β_c on $\phi(\eta)$ & $\phi_p(\eta)$.

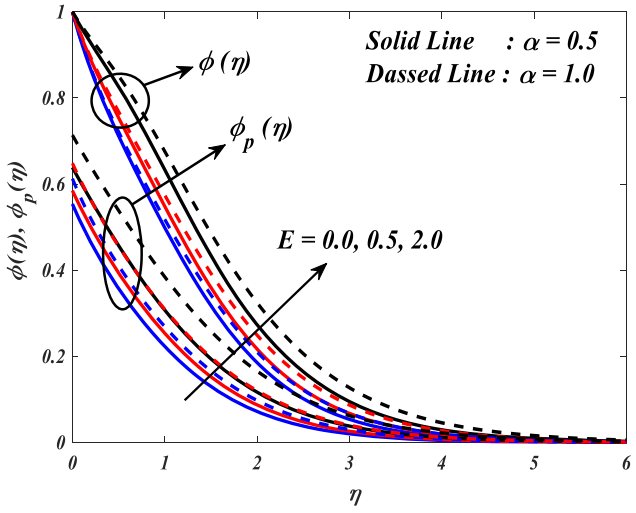

Figure 15: Influence of E on $\phi(\eta)$ & $\phi_p(\eta)$.

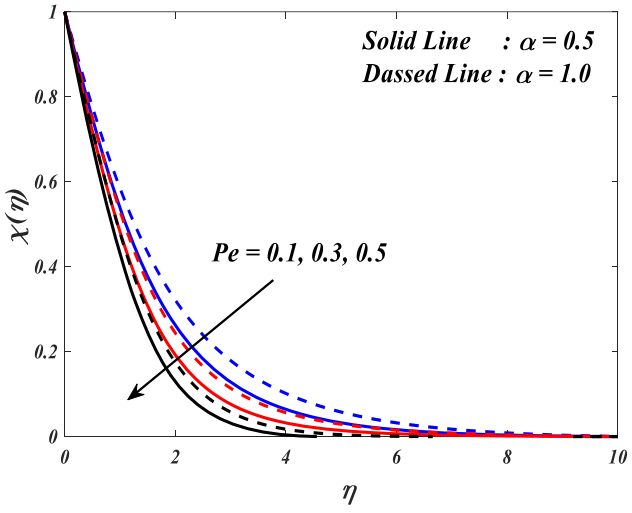

Figure 18: Influence of Pe on $\chi(\eta)$.

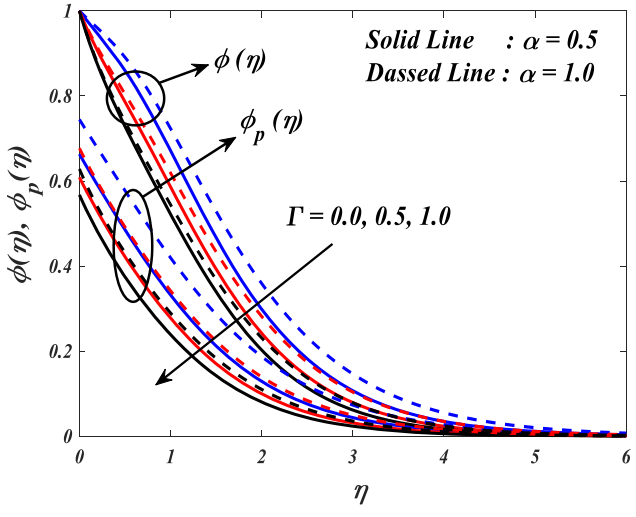

Figure 16: Influence of Γ on $\phi(\eta)$ & $\phi_p(\eta)$.

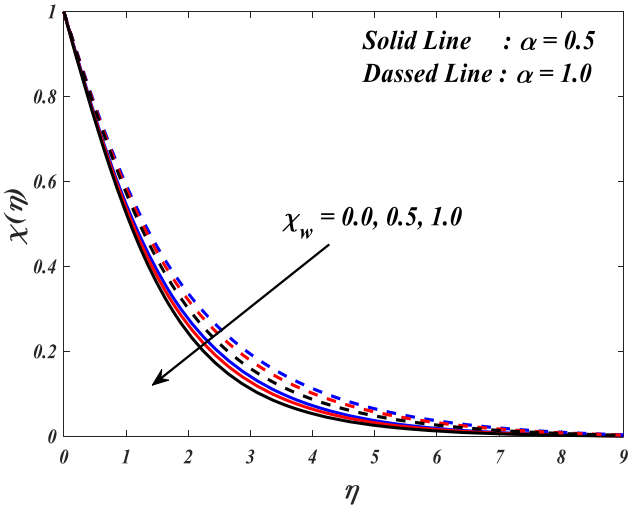

Figure 19: Influence of χ_w on $\chi(\eta)$.

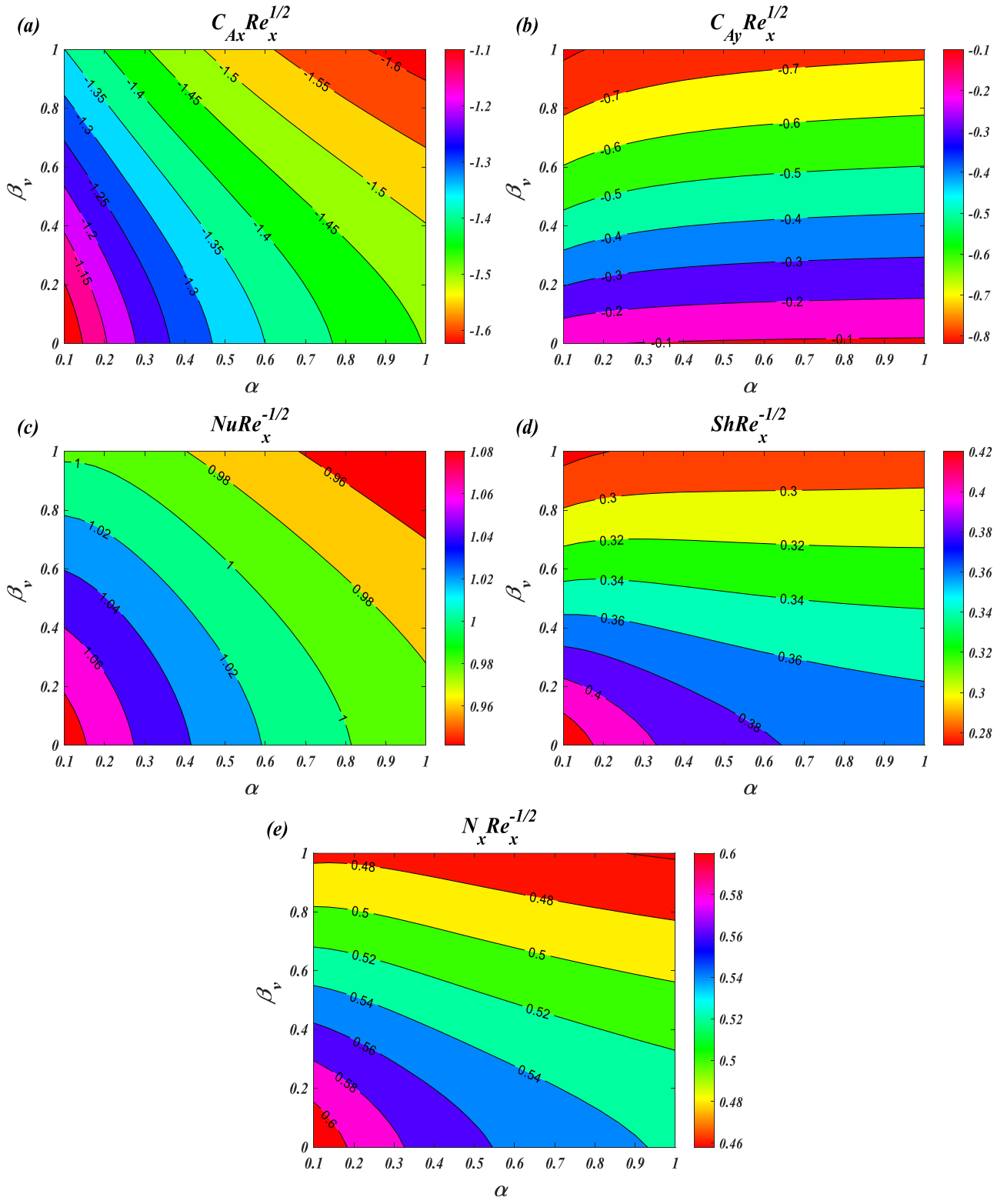

Figure 20: Influence of β_v and α on (a) $C_{Ax}\,\mathrm{Re}_x^{1/2}$, (b) $C_{Ay}\,\mathrm{Re}_x^{1/2}$, (c) $\mathrm{Nu}\,\mathrm{Re}_x^{-1/2}$, (d) $\mathrm{Sh}\,\mathrm{Re}_x^{-1/2}$, and (e) $N_x\,\mathrm{Re}_x^{-1/2}$.

parameter (E). An activation energy that is much higher than average leads the Arrhenius function to slope upward, which in turn increases the efficiency of the chemical process. As a consequence of this, the concentration of nanoparticles increases. Physically, stronger molecular connections and reaction rates are made possible by larger activation energies, which enable more nanoparticles to remain in the system rather than dissipate. As a consequence, the concentration distribution across the fluid medium becomes more noticeable.

5.10 Effect of chemical reaction (Γ)

Various values of the chemical reaction parameter (Γ) are shown in Figure 16, which illustrates the oscillations that occur in a ($\phi(\eta)$ & $\phi_p(\eta)$). As a result of increasing the values of the chemical reaction parameter (Γ), it has been seen that the ($\phi(\eta)$ & $\phi_p(\eta)$) profiles are increasing. The concentration of liquid species decreases because they dissolve more efficiently. The acceleration of species dissolution that results from a greater chemical reaction parameter leads to a decrease in fluid concentration.

5.11 Effect of fluid–particle interaction (β_c)

Figure 17 shows the concentration profile ($\phi(\eta)$ & $\phi_p(\eta)$) with various fluid–particle interaction parameter for concentration (β_c) values approaching both (α = 0.5) and (α = 1). Fluid concentration ($\phi(\eta)$) decreased while DNF ($\phi_p(\eta)$) increased at higher values of (β_c). When the interactions between particles and fluids are stronger, the concentration of base fluid decreases while the concentration of DNF increases.

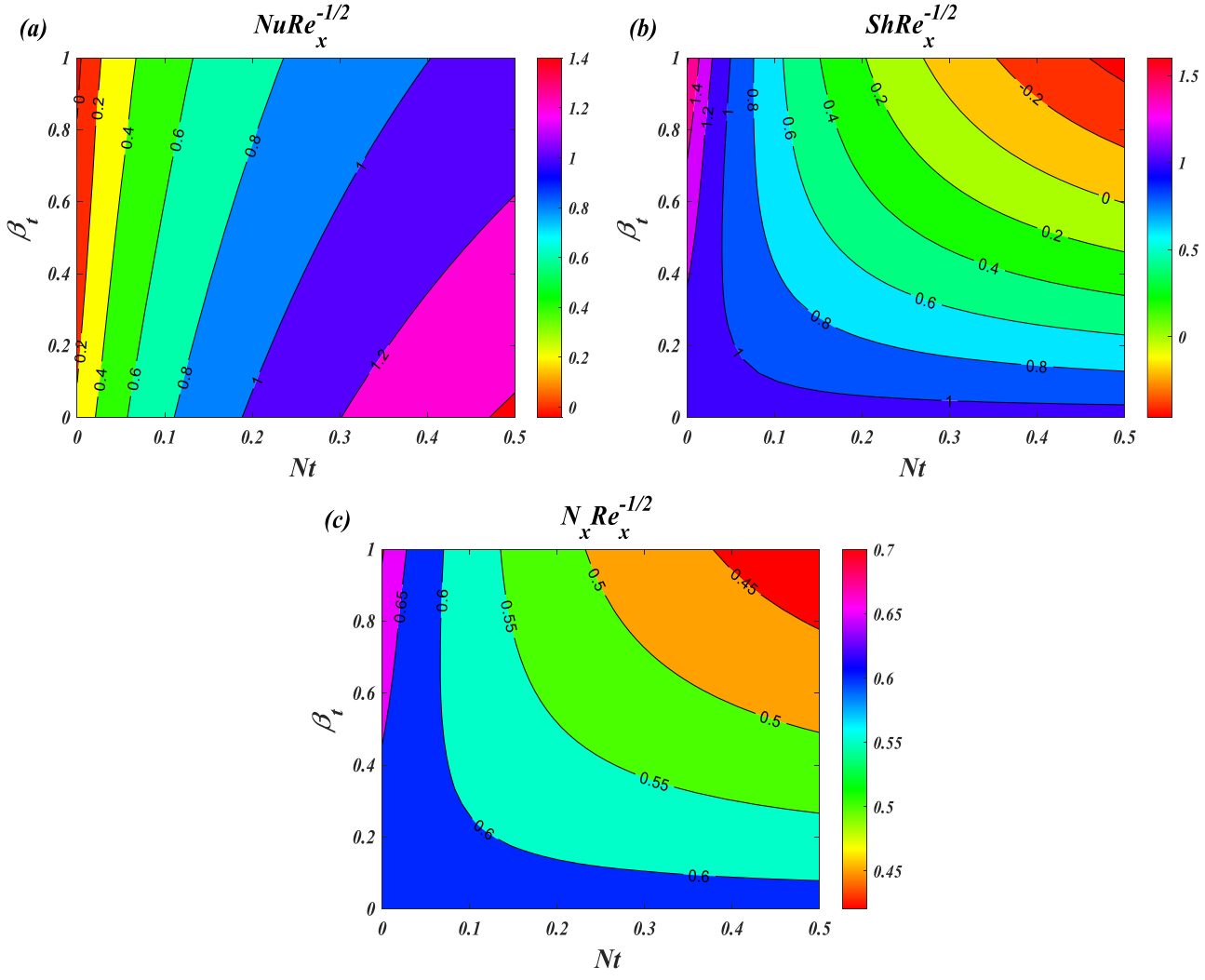

Figure 21: Influence of β_t and Nt on (a) $\mathrm{Nu}\,\mathrm{Re}_x^{-1/2}$, (b) $\mathrm{Sh}\,\mathrm{Re}_x^{-1/2}$, and (c) $N_x\,\mathrm{Re}_x^{-1/2}$.

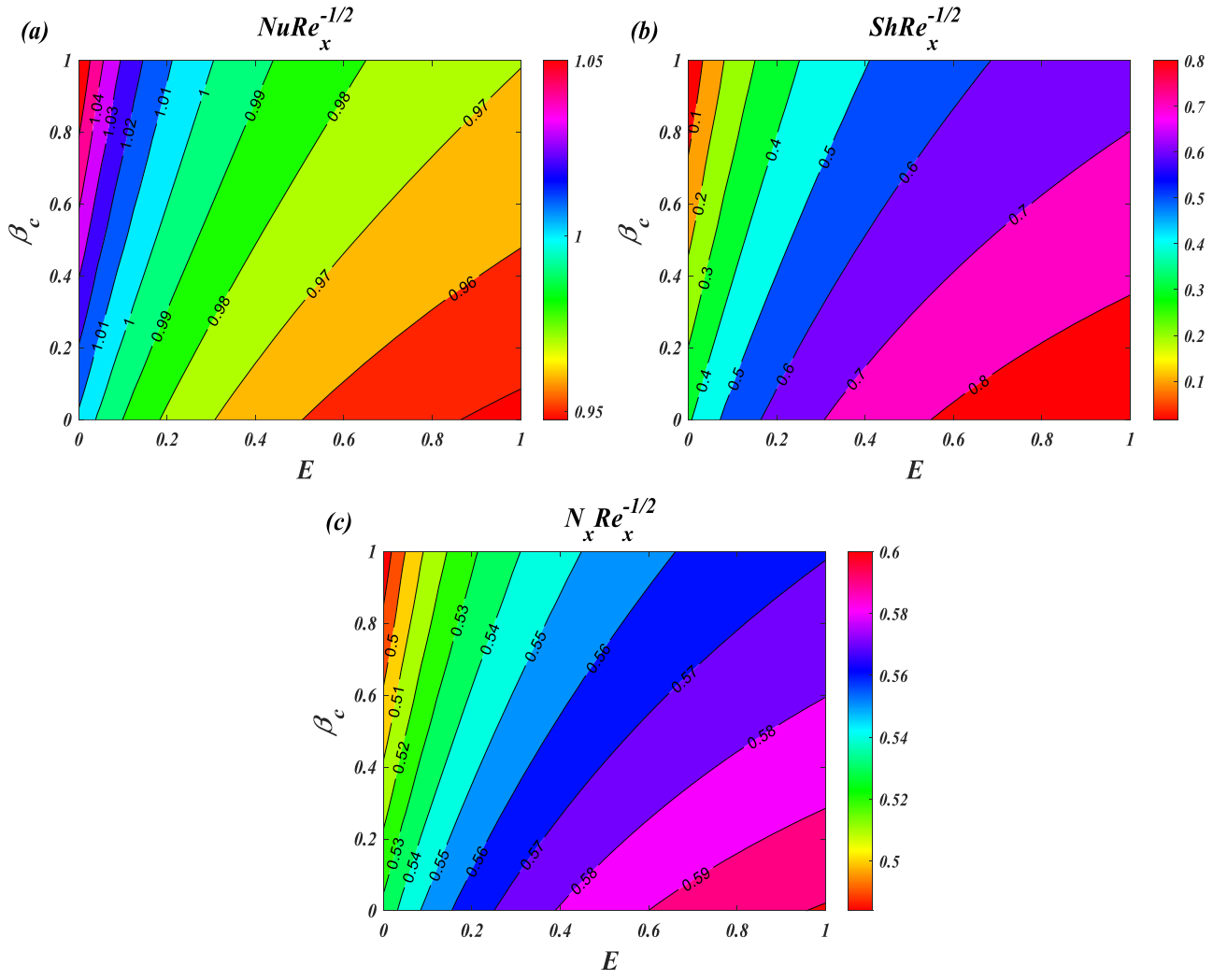

Figure 22: Influence of β_c and E on (a) $\mathrm{Nu}\,\mathrm{Re}_x^{-1/2}$, (b) $\mathrm{Sh}\,\mathrm{Re}_x^{-1/2}$, and (c) $N_x\,\mathrm{Re}_x^{-1/2}$.

5.12 Effect of Peclet number (Pe)

An illustration of the effect that the Peclet number (Pe) has on the microbe density ($\chi(\eta)$) can be seen in Figure 18. Therefore, higher values of the (Pe) parameter result in a reduction in the density and fluid mass of the surrounding environment. There is a decrease in the microbe density when there is an increase in the Peclet number. This indicates that there is an increase in convective transport, which in turn lowers the accumulation of germs in the fluid.

5.13 Effect of microorganism density (χ_w)

The influence of microorganism density (χ_w) on ($\chi(\eta)$) is seen in Figure 19. Therefore, the microorganism density is reduced when the (χ_w) parameter's value increases. As the microorganism density parameter rises, the concentration of motile microbes falls. This is because of increased motility and dispersion, which ultimately results in a lower accumulation of microorganisms in the fluid.

5.14 Effect of skin friction ($C_{Ax}\mathrm{Re}_x^{1/2}$) & ($C_{Ay}\mathrm{Re}_x^{1/2}$), Nusselt number ($\mathrm{Nu}\ \mathrm{Re}_x^{-1/2}$), mass transfer rate ($\mathrm{Sh}\ \mathrm{Re}_x^{-1/2}$), and motile microorganism

Figure 20(a–e) is shown in order to demonstrate the impact of the fluid–particle interaction parameter (β_v) and rotational parameter (α) on (a and b) skin friction ($C_{Ax}\,\mathrm{Re}_x^{1/2}$) & ($C_{Ay}\,\mathrm{Re}_x^{1/2}$), (c) Nusselt number ($\mathrm{Nu}\,\mathrm{Re}_x^{-1/2}$), (d)

mass transfer rate ($\mathrm{Sh}\,\mathrm{Re}_x^{-1/2}$), and (e) motile microorganism of local density number ($N_x\,\mathrm{Re}_x^{-1/2}$). It is observed that decreases in the ($C_{Ax}\,\mathrm{Re}_x^{1/2}$) nanofluid over the surface affects the (β_v) and (α) parameters. It is seen that ($C_{Ay}\,\mathrm{Re}_x^{1/2}$) increases for increasing values of (β_v) and (α). Figure 20(c) shows that the rate of heat transfer ($\mathrm{Nu}\,\mathrm{Re}_x^{-1/2}$) decreases for higher values of (β_v) and (α). In Figure 20(d), it is observed that higher values of (β_v) enhance ($\mathrm{Sh}\,\mathrm{Re}_x^{-1/2}$) , while higher values of (α) cause a decrease. The larger values of the (β_v) increase ($N_x\,\mathrm{Re}_x^{-1/2}$) but mandate the higher (α) values, as seen in Figure 20(e). Figure 21(a–c) analyzes the impact of the fluid–particle interaction parameter for temperature (β_t) and thermophoresis (Nt) on (a) Nusselt number ($\mathrm{Nu}\,\mathrm{Re}_x^{-1/2}$), (b) mass transfer rate ($\mathrm{Sh}\,\mathrm{Re}_x^{-1/2}$), and (c) motile microorganism of local density number ($N_x\,\mathrm{Re}_x^{-1/2}$). From Figure 21(a), it can be observed that the rate of heat transfer ($\mathrm{Nu}\,\mathrm{Re}_x^{-1/2}$) increases with the higher values of (β_t) and (Nt). As shown in Figure 21(b), ($\mathrm{Sh}\,\mathrm{Re}_x^{-1/2}$) increases with higher values of (β_t) but decreases with the higher (Nt) values. As seen in Figure 21(c), larger (β_t) values enhance ($N_x\,\mathrm{Re}_x^{-1/2}$), whereas increased (Nt) values lead to a decrease. The impact of the fluid–particle interaction parameter for concentration (β_c) and activation energy (E) on (a) Nusselt number ($\mathrm{Nu}\,\mathrm{Re}_x^{-1/2}$), (b) mass transfer rate ($\mathrm{Sh}\,\mathrm{Re}_x^{-1/2}$), and (c) motile microorganism of local density number ($N_x\,\mathrm{Re}_x^{-1/2}$) is presented in Figure 22(a–c). Figure 22(a) shows that the rate of heat transfer ($\mathrm{Nu}\,\mathrm{Re}_x^{-1/2}$) increases for the higher values of the (β_c) and (E). It can be observed from Figure 22(b) that the rate of mass transfer ($\mathrm{Sh}\,\mathrm{Re}_x^{-1/2}$) increases with the increase in (β_c) and (E) values. The motile microorganism of local density number ($N_x\,\mathrm{Re}_x^{-1/2}$) is known to increase with the increasing values of (β_c) and (E) according to Figure 22(c).

6 Conclusion

This study demonstrates the efficacy of a multi-layer ANN in analyzing the effects of the Coriolis force and activation energy on the flow of a DNF containing gyrotactic microorganisms over a three-dimensional sheet. The study also considers the influence of linear thermal radiation and a non-uniform heat source on the system. The results are presented in two-dimensional graphs, revealing the following key findings:

- The ANN methodology effectively reduces computational time when solving complex fluid dynamics problems.
- The dust fluid velocity ($g_1'(\eta)$) increases with higher values of the fluid–particle interaction parameter, whereas the fluid velocity ($G_1'(\eta)$) decreases.
- The temperature ($\theta(\eta)$ & $\theta_p(\eta)$) and concentration profiles ($\phi(\eta)$ & $\phi_p(\eta)$) decrease with increasing values of mass concentration of dusty particles (I).
- Higher values of the thermophoresis parameter (Nt) enhance both temperature and concentration profiles.
- An increase in the Brownian motion parameter (Nb) increases the temperature ($\theta(\eta)$ & $\theta_p(\eta)$) but decreases the concentration ($\phi(\eta)$ & $\phi_p(\eta)$).
- The microorganism density ($\chi(\eta)$) decreases with the higher values of the concentration ratio parameter (χ_w).
- The rate of heat transfer ($\mathrm{Nu}\,\mathrm{Re}_x^{-1/2}$) increases with the higher values of (β_t) and (Nt).

The findings have practical implications in geothermal energy extraction, industrial cooling systems, wastewater treatment, and enhanced oil recovery. For instance, in geothermal power plants, optimizing nanofluid properties can improve heat transfer efficiency, reducing energy consumption. Similarly, in wastewater treatment, understanding microorganism dynamics helps in bacterial control, improving purification efficiency. These insights contribute to sustainable and efficient thermal management solutions across industries. Future investigations may include hybrid nanofluids, magnetohydrodynamic effects, and experimental validation using CFDs and deep learning. Current constraints include constant property assumptions, nanoparticle aggregation, and the lack of empirical validation.

Acknowledgments: This work was supported by the Government wide R&D Fund Infectious Disease Research (GFID), with a grant funded by the government of the Republic of Korea (Ministry of Health and welfare), Korea Health Industry Development Institute (KHIDI) (The development of infection control and prevention technologies for strengthening the infection control capacity of medical institutions), under Grant RS-2025-02310471.

Funding information: This work was supported by the Government wide R&D Fund Infectious Disease Research (GFID), with a grant funded by the government of the Republic of Korea (Ministry of Health and welfare), Korea Health Industry Development Institute (KHIDI) (The development of infection control and prevention technologies for strengthening the infection control capacity of medical institutions), under Grant RS-2025-02310471.

Author contributions: All authors have accepted responsibility for the entire content of this manuscript and approved its submission.

Conflict of interest: The authors state no conflict of interest.

Data availability statement: All data generated or analyzed in this study are fully presented within this published article.

References

[1] Rashed AS, Mahmoud TA, Mabrouk SM. Enhanced flow and temperature profiles in ternary hybrid nanofluid with gyrotactic microorganisms: a study on magnetic field, brownian motion, and thermophoresis phenomena. J Appl Comput Mech. 2024;10:597–609. doi: 10.22055/jacm.2024.45899.4427.

[2] Atif SM, Hussain S, Sagheer M. Magnetohydrodynamic stratified bioconvective flow of micropolar nanofluid due to gyrotactic microorganisms. AIP Adv. 2019;9:025208. doi: 10.1063/1.5085742.

[3] Begum N, Siddiqa S, Sulaiman M, Islam S, Hossain MA, Gorla RSR. Numerical solutions for gyrotactic bioconvection of dusty nanofluid along a vertical isothermal surface. Int J Heat Mass Transf. 2017;113:229–36. doi: 10.1016/j.ijheatmasstransfer.2017.05.071.

[4] Agarwal P, Jain R, Loganathan K. Thermally radiative flow of MHD Powell-Eyring nanofluid over an exponential stretching sheet with swimming microorganisms and viscous dissipation: A numerical computation. Int J Thermofluids. 2024;23:100773. doi: 10.1016/j.ijft.2024.100773.

[5] Rajeswari PM, De P. Multi-stratified effects on stagnation point nanofluid flow with gyrotactic microorganisms over porous medium. J Porous Media. 2024;27:67–84. doi: 10.1615/JPorMedia.2023050040.

[6] Jakeer S, Polu BAR. Homotopy perturbation method solution of magneto-polymer nanofluid containing gyrotactic microorganisms over the permeable sheet with Cattaneo–Christov heat and mass flux model. Proc Inst Mech Eng Part E J Process Mech Eng. 2021;236:525–34. doi: 10.1177/09544089211048993.

[7] Basha HT, Sivaraj R. Numerical simulation of blood nanofluid flow over three different geometries by means of gyrotactic microorganisms: Applications to the flow in a circulatory system. Proc Inst Mech Eng Part C J Mech Eng Sci. 2021;235:441–60. doi: 10.1177/0954406220947454.

[8] Alharbi FM, Naeem M, Zubair M, Jawad M, Jan WU, Jan R. Bioconvection due to gyrotactic microorganisms in couple stress hybrid nanofluid laminar mixed convection incompressible flow with magnetic nanoparticles and chemical reaction as carrier for targeted drug delivery through porous stretching sheet. Molecules. 2021;26:3954. doi: 10.3390/molecules26133954.

[9] Waqas H, Kamran T, Imran M, Muhammad T. MHD bioconvectional flow of Jeffrey nanofluid with motile microorganisms over a stretching sheet: solar radiation applications. Waves Random Complex Media. 2022;1–30. doi: 10.1080/17455030.2022.2105418.

[10] Mehmood Z, Iqbal Z. Interaction of induced magnetic field and stagnation point flow on bioconvection nanofluid submerged in gyrotactic microorganisms. J Mol Liq. 2016;224:1083–91. doi: 10.1016/j.molliq.2016.10.014.

[11] Kuznetsov AV. The onset of nanofluid bioconvection in a suspension containing both nanoparticles and gyrotactic microorganisms. Int Commun Heat Mass Transf. 2010;37:1421–5. doi: 10.1016/j.icheatmasstransfer.2010.08.015.

[12] Ahmad S, Akhter S, Imran Shahid M, Ali K, Akhtar M, Ashraf M. Novel thermal aspects of hybrid nanofluid flow comprising of manganese zinc ferrite MnZnFe2O4, nickel zinc ferrite $NiZnFe_2O_4$ and motile microorganisms. Ain Shams Eng J. 2022;13:101668. doi: 10.1016/j.asej.2021.101668.

[13] Dey D, Chutia B. Dusty nanofluid flow with bioconvection past a vertical stretching surface. J King Saud Univ – Eng Sci. 2022;34:375–80. doi: 10.1016/j.jksues.2020.11.001.

[14] Rajeswari PM, De P. Shape factor and sensitivity analysis on stagnation point of bioconvective tetra-hybrid nanofluid over porous stretched vertical cylinder. Bionanoscience. 2024;14:3035–58. doi: 10.1007/s12668-024-01586-8.

[15] Loganathan K, Jain R, Eswaramoorthi S, Abbas M, Alqahtani MS. Bioconvective gyrotactic microorganisms in third-grade nanofluid flow over a Riga surface with stratification: An approach to entropy minimization. Open Phys. 2023;21:20230273. doi: 10.1515/phys-2023-0273.

[16] Loganathan K, Alessa N, Jain R, Ali F, Zaib A. Dynamics of heat and mass transfer: Ree-Eyring nanofluid flow over a Riga plate with bioconvention and thermal radiation. Front Phys. 2022;10:974562. doi: 10.3389/fphy.2022.974562.

[17] Rashed AS, Nasr E, Mabrouk SM. Bioconvective flow surrounding a thin surgical needle in blood incorporating ternary hybrid nanoparticles. Comput Methods Differ Equations. 2024. doi: 10.22034/CMDE.2024.61425.2643.

[18] Fortov VE, Vaulina OS, Petrov OF, Vasiliev MN, Gavrikov AV, Shakova IA, et al. Experimental study of the heat transport processes in dusty plasma fluid. Phys Rev E – Stat Nonlinear, Soft Matter Phys. 2007;75:026403. doi: 10.1103/PhysRevE.75.026403.

[19] Basha HT, Kim H, Jang B. Buoyancy-driven heat transfer and entropy analysis of a hydromagnetic GO-Fe3O4/H2O hybrid nanofluid in an energy storage enclosure partially filled with non-Darcy porous medium under an oblique magnetic field. Int J Numer Methods Heat Fluid Flow. 2024;35:491–523. doi: 10.1108/HFF-03-2024-0193/FULL/XML.

[20] Basha HT, Jang B. Machine learning analysis for heat transfer enhancement in nano-encapsulated phase change materials within L-shaped enclosure with heated blocks. Appl Therm Eng. 2025;259:124803. doi: 10.1016/J.APPLTHERMALENG.2024.124803.

[21] Jakeer S, Reddy PBA. Entropy generation on the variable magnetic field and magnetohydrodynamic stagnation point flow of Eyring–Powell hybrid dusty nanofluid: Solar thermal application. Proc Inst Mech Eng Part C J Mech Eng Sci. 2022;236:7442–55. doi: 10.1177/09544062211072457.

[22] Lou Q, Ali B, Rehman SU, Habib D, Abdal S, Shah NA, et al. Micropolar dusty fluid: Coriolis force effects on dynamics of MHD rotating fluid when Lorentz force is significant. Mathematics. 2022;10:1–13. doi: 10.3390/math10152630.

[23] Kalpana G, Madhura KR, Kudenatti RB. Impact of temperature-dependant viscosity and thermal conductivity on MHD boundary layer flow of two-phase dusty fluid through permeable medium.

Eng Sci Technol Int J. 2019;22:416–27. doi: 10.1016/j.jestch.2018.10.009.
[24] Mahdy A, Hoshoudy GA. Two-phase mixed convection nanofluid flow of a dusty tangent hyperbolic past a nonlinearly stretching sheet. J Egypt Math Soc. 2019;27:44. doi: 10.1186/s42787-019-0050-9.
[25] Ramana Reddy JV, Sugunamma V, Sandeep N. Thermophoresis and Brownian motion effects on unsteady MHD nanofluid flow over a slendering stretching surface with slip effects. Alex Eng J. 2018;57:2465–73. doi: 10.1016/j.aej.2017.02.014.
[26] Ghadikolaei SS, Hosseinzadeh K, Hatami M, Ganji DD. MHD boundary layer analysis for micropolar dusty fluid containing Hybrid nanoparticles (Cu-Al2O3) over a porous medium. J Mol Liq. 2018;268:813–23. doi: 10.1016/J.MOLLIQ.2018.07.105.
[27] Gnaneswara Reddy M, Sudha Rani MVVNL, Ganesh Kumar K, Prasannakumar BC, Lokesh HJ. Hybrid dusty fluid flow through a Cattaneo–Christov heat flux model. Phys A Stat Mech Its Appl. 2020;511:123975. doi: 10.1016/j.physa.2019.123975.
[28] Imitaz A, Aamina A, Ali F, Khan I, Nisar KS. Two-phase flow of blood with magnetic dusty particles in cylindrical region: A Caputo-Fabrizio fractional model. Comput Mater Contin. 2020;66:2253–64. doi: 10.32604/cmc.2021.012470.
[29] Nawaz M, Madkhali HA, Haneef M, Alharbi SO, Alaoui MK. Numerical study on thermal enhancement in hyperbolic tangent fluid with dust and hybrid nanoparticles. Int Commun Heat Mass Transf. 2021;127:105535. doi: 10.1016/j.icheatmasstransfer.2021.105535.
[30] De MA. Comparative study of hybrid, tri-hybrid and tetra-hybrid nanoparticles in MHD unsteady flow with chemical reaction, activation energy, Soret-Dufour effect and sensitivity analysis over non-Darcy porous stretching cylinder. Heliyon. 2024;10:e35731. doi: 10.1016/j.heliyon.2024.e35731.
[31] Khan MI, Hayat T, Khan MI, Alsaedi A. Activation energy impact in nonlinear radiative stagnation point flow of cross nanofluid. Int Commun Heat Mass Transf. 2018;91:216–24. doi: 10.1016/j.icheatmasstransfer.2017.11.001.
[32] Hayat T, Riaz R, Aziz A, Alsaedi A. Influence of Arrhenius activation energy in MHD flow of third grade nanofluid over a nonlinear stretching surface with convective heat and mass conditions. Phys A Stat Mech Appl. 2020;549:124006. doi: 10.1016/j.physa.2019.124006.
[33] Lian W, Wang J, Wang G, Gao D, Li X, Zhang Z, et al. Investigation on the lignite pyrolysis reaction kinetics based on the general Arrhenius formula. Fuel. 2020;268:117364. doi: 10.1016/j.fuel.2020.117364.
[34] Khan MI, Qayyum S, Hayat T, Waqas M, Imran M, Alsaedi A. Entropy generation minimization and binary chemical reaction with Arrhenius activation energy in MHD radiative flow of nanomaterial. J Mol Liq. 2018;259:274–83. doi: 10.1016/j.molliq.2018.03.049.
[35] Khan MI, Ahmad MW, Alsaedi A, Hayat T. Entropy generation optimization in flow of non-Newtonian nanomaterial with binary chemical reaction and Arrhenius activation energy. Phys A. 2020;538:122806. doi: 10.1016/j.physa.2019.122806.
[36] Shafique Z, Mustafa M, Mushtaq A. Boundary layer flow of Maxwell fluid in rotating frame with binary chemical reaction and activation energy. Results Phys. 2016;6:627–33. doi: 10.1016/j.rinp.2016.09.006.
[37] Reddy SRR, Bala Anki Reddy P, Bhattacharyya K. Effect of nonlinear thermal radiation on 3D magneto slip flow of Eyring-Powell nanofluid flow over a slendering sheet with binary chemical reaction and Arrhenius activation energy. Adv Powder Technol. 2019;30:3203–13. doi: 10.1016/j.apt.2019.09.029.
[38] Gomathi N, Poulomi D. Dual solutions of Casson Williamson nanofluid with thermal radiation and chemical reaction. Numer Heat Transf Part A Appl. 2024;1–24. doi: 10.1080/10407782.2024.2326980.
[39] Mabrouk SM, Inc M, Rashed AS, Akgül A. Similarity analysis of bioconvection of unsteady nonhomogeneous hybrid nanofluids influenced by motile microorganisms. J Biol Phys. 2024;50:119–48. doi: 10.1007/s10867-023-09651-1.
[40] Reddy SRR, Jakeer S, Rupa ML. ANN model of three-dimensional micropolar dusty hybrid nanofluid flow with Coriolis force: biomedical applications. Indian J Phys. 2023;97:3801–25. doi: 10.1007/s12648-023-02737-5.
[41] Jakeer S, Rupa ML, Reddy SRR, Rashad AM. Artificial neural network model of non-Darcy MHD Sutterby hybrid nanofluid flow over a curved permeable surface: Solar energy applications. Propuls Power Res. 2023;12:410–27. doi: 10.1016/j.jppr.2023.07.002.
[42] Rehman SU, Mariam A, Ullah A, Asjad MI, Bajuri MY, Pansera BA, et al. Numerical computation of buoyancy and radiation effects on MHD micropolar nanofluid flow over a stretching/shrinking sheet with heat source. Case Stud Therm Eng. 2021;25:100867. doi: 10.1016/J.CSITE.2021.100867.
[43] Ali B, Nie Y, Khan SA, Sadiq MT, Tariq M. Finite element simulation of multiple slip effects on MHD unsteady Maxwell nanofluid flow over a permeable stretching sheet with radiation and thermo-diffusion in the presence of chemical reaction. Processes. 2019;7:628. doi: 10.3390/PR7090628.